



HAL
open science

Constraining the Earth's Dynamical Ellipticity From Ice Age Dynamics

Mohammad Farhat, Jacques Laskar, Gwenaël. Boué

► **To cite this version:**

Mohammad Farhat, Jacques Laskar, Gwenaël. Boué. Constraining the Earth's Dynamical Ellipticity From Ice Age Dynamics. *Journal of Geophysical Research: Solid Earth*, 2022, 127, 10.1029/2021JB023323 . insu-03718983

HAL Id: insu-03718983

<https://insu.hal.science/insu-03718983>

Submitted on 11 May 2023

HAL is a multi-disciplinary open access archive for the deposit and dissemination of scientific research documents, whether they are published or not. The documents may come from teaching and research institutions in France or abroad, or from public or private research centers.

L'archive ouverte pluridisciplinaire **HAL**, est destinée au dépôt et à la diffusion de documents scientifiques de niveau recherche, publiés ou non, émanant des établissements d'enseignement et de recherche français ou étrangers, des laboratoires publics ou privés.

Copyright

JGR Solid Earth

RESEARCH ARTICLE

10.1029/2021JB023323

Key Points:

- We trace the variation in the Earth's dynamical ellipticity in the context of the Earth's viscoelastic deformation during Cenozoic ice ages
- Its perturbation is well constrained within [−0.13%, 0.07%] over the last 3 Myr, and within [−0.11%, 0.05%] over the rest of the Cenozoic
- These dynamical ellipticity variations are a key element in the computation of the long term evolution of the Earth's rotational motion

Correspondence to:

M. Farhat,
mohammad.farhat@obspm.fr

Citation:

Farhat, M., Laskar, J., & Boué, G. (2022). Constraining the Earth's dynamical ellipticity from ice age dynamics. *Journal of Geophysical Research: Solid Earth*, 127, e2021JB023323. <https://doi.org/10.1029/2021JB023323>

Received 6 APR 2021
 Accepted 6 MAY 2022

Constraining the Earth's Dynamical Ellipticity From Ice Age Dynamics

Mohammad Farhat¹ , Jacques Laskar¹ , and Gwenaél Boué¹

¹IMCCE, CNRS, Observatoire de Paris, PSL University, Sorbonne Université, Paris, France

Abstract The dynamical ellipticity of a planet expresses the departure of its mass distribution from spherical symmetry. It enters as a parameter in the description of a planet's precession and nutation, as well as other rotational normal modes. In the case of the Earth, uncertainties in this quantity's history produce an uncertainty in the solutions for the past evolution of the Earth-Moon system. Constraining this history has been a target of interdisciplinary efforts as it represents an astro-geodetic parameter whose variation is shaped by geophysical processes, and whose imprints can be found in the geological signal. We revisit the classical problem of its variation during ice ages, where glacial cycles exerted a varying surface loading that had altered the shape of the geoid. In the framework of glacial isostatic adjustment, and with the help of a recent paleoclimatic proxy of ice volume, we present the evolution of the dynamical ellipticity over the Cenozoic ice ages. We map out the problem in full generality identifying major sensitivities to surface loading and internal variations in parameter space. This constrained evolution is aimed to be used in future astronomical computations of the orbital and insolation quantities of the Earth.

Plain Language Summary The Earth is a deformable body subject to inner, surface, and outer forces acting together to adjust its mass distribution. This mass distribution is quantified by the dynamical ellipticity, and its evolution is largely unknown over geological timescales. As this parameter plays an important role in the evolution of the Earth's rotational motion, its uncertainty propagates to long term solutions of the Earth's orientation. To minimize this uncertainty, we present here a solution of the Earth's dynamical ellipticity over the past 50 Myr, pertaining to the surface loading contribution of the Cenozoic glacial cycles. We do so by combining oceanic proxies of glacial volume with the proper mathematical formalism to reconstruct a self-consistent history of the glacial and oceanic loading. As the Earth's response to this loading is highly dependent on its viscosity, we perform a parametric study and constrain the possible scenarios of dynamical ellipticity evolution. Combined with other processes involving mass redistribution, such as mantle convection and the tidal response, our findings add a missing puzzle piece toward a complete history of the dynamical ellipticity, and consequently valid extended rotational solutions.

1. Introduction

Cyclostratigraphy and astronomical tuning have opened a new era where geological time scales can be constrained by the orbital and rotational motion of the solar system (e.g., Gradstein et al., 2004, 2012, 2020). This relies on the possibility of obtaining an accurate solution for the motion of the Earth over several millions of years (Myr). At present, reliable orbital solutions have been obtained for the solar system over about 50 Myr (Laskar, Fienga, et al., 2011; Laskar et al., 2004), and we know that extending the validity of the solution beyond this limit is hindered by the chaotic behavior of the solar system (Laskar, 1989; Laskar, Gastineau, et al., 2011). In contrast, the validity of the precession and obliquity solutions of the Earth is much more limited, to about 10–20 Myr (Laskar et al., 2004). This is due to several uncertainties that arise in the computation of the past rotational evolution of the Earth. Namely, uncertainties pertaining to the time variation of tidal dissipation in the Earth-Moon system (e.g., Neron de Surgy & Laskar, 1997) and the deformation of the Earth due to mantle convection (Forte et al., 1993) or due to the varying surface load during the past ice ages (e.g., Ghelichkhan et al., 2020; Levrard & Laskar, 2003; Peltier & Jiang, 1994). The present work addresses this latter contribution. It is a key component for the establishment of a precise computation of the rotational and precession state of the Earth over the past 60 Myr.

The ellipsoidal flattening of the Earth, estimated to be around $1/299.8$ (Chambat et al., 2010), is primarily a property of the mass distribution resulting from the hydrostatic competition between the dominant gravitational force and the weaker centrifugal force. Present observational inference of this quantity reports an excess in the

flattening of 0.5%, corresponding to a difference between the equatorial and polar radii that is 110 m larger than equilibrium (Chambat et al., 2010; Stacey & Davis, 2008) (much less than the analogous flattening of $\sim 3.8\%$ at the core-mantle boundary (Mathews et al., 2002)). This excess is also observed to be decreasing in an attempt of recovering the equilibrium figure (Cox & Chao, 2002). Mechanisms driving this excess vary in nature, magnitude, and time scales (Morrow et al., 2012). They range from astronomical forcing leading to a variation in the gravitational potential between the equator and the poles and tidal friction, to geophysical mechanisms pertaining to surface and internal adjustment in response to the mantle heterogeneity or to surface loading. The net outcome is altering the Earth's rotational motion and consequently the Milankovitch band cyclicity in proxy records (Levrard & Laskar, 2003; Peltier, 1983; Stephenson, 2008).

As a measure of the difference between the polar and equatorial moments of inertia, the dynamical ellipticity is a global parameter that drives the precession and nutation of the Earth. The difficulty in tracing its history over geological timescales is one of the major sources of uncertainty in determining the evolution of the Earth's obliquity and precession (Laskar et al., 1993, 2004). In the last decades, proxy records corresponding to the recent millions of years have been used to attempt constraining the dynamical ellipticity variation (Lourens et al., 2001; Pälike & Shackleton, 2000).

We focus here on ice ages, during which cycles of glaciation and deglaciation exert a varying surface load upon the Earth's lithosphere due to the movement of water between the ice caps and the oceans. This load forces the Earth to deform by subsiding under the growing load and rebounding upon its decay. However, this deformation is constrained by re-establishing an equilibrium between the deformation of the lithosphere and the underlying mantle; a state that is classically coined as isostatic equilibrium. Thus glacial isostatic adjustment (GIA) describes the process of isostatic deformation due to ice and water surface loading variation. As a result of glaciation, surface mass is transferred into the poles and the dynamical ellipticity is reduced. This direct effect of glaciation is partially compensated by the delayed effect of GIA attempting to re-balance the inertia budget. The opposite occurs during deglaciation periods.

The influence of recent glacial cycles on the dynamical ellipticity have been first addressed outside the scope of GIA using simplified models of surface loading on a rigid Earth (Berger, 1988; Dehant et al., 1990; Thomson, 1990). The results are upper bound limits that cannot be attained in the context of a realistic Earth model, but were sufficient to the community at that time. More elaborate and meticulous approaches to the problem were motivated by the analysis of Laskar et al. (1993) suggesting a possible resonance crossing with Jupiter and Saturn if the dynamical ellipticity is perturbed by a factor of -0.223% relative to its present value. This called for a sequence of works that used climatic proxy records over the past million years to constrain the glacial surface loading, and the developed theory of the viscoelastic response of the Earth (Mitrović & Forte, 1995; Mitrović et al., 1997; Peltier & Jiang, 1994). All studies concluded with the unlikelihood of occurrence of such an event. The problem was recently addressed again covering the past 3 Myr corresponding to the interval of maximum glacial volumetric loading and continental spread over the surface of the Earth (Ghelichkhan et al., 2020).

In this work, we first elaborate on the dynamical nature of a possible resonance between the Earth, Jupiter, and Saturn due to variations in the Earth's dynamical ellipticity (Section 2). We then revisit the problem equipped with all the developments of the GIA theory pertaining to the viscoelastic deformation of the Earth and the self-consistent connection of the glacial/oceanic surface loading using the sea level equation (SLE) formalism (Section 3). We use a very recent proxy record covering the Cenozoic era (Miller et al., 2020). This allows us to build a model of glacial loading variation over an extended interval of time (Section 4). Combining these two elements, we trace the variation of the perturbation in dynamical ellipticity by a set of numerical simulations of the sea level variation (Section 5). We then map out the problem in full generality in an attempt to constrain its variables.

2. The Dynamical Ellipticity and the $s_6 - g_6 + g_5$ Resonance

Besides our aim to minimize uncertainties in the computation of the precession and obliquity evolution of the Earth, we are interested in certain behaviors of the dynamical ellipticity that can force the Earth into scenarios involving significant obliquity variations. The possibility of such scenarios was first discovered and examined by Laskar et al. (1993), and we delineate in this brief section on the dynamical origin of it.

The dynamical ellipticity of the Earth is a measure of the difference between the polar moment of inertia C and the equatorial moments of inertia A and B , namely:

$$H = \frac{C - (A + B)/2}{C}. \quad (1)$$

It can also be written as a linear function of the gravitational second zonal harmonic J_2 :

$$H = \frac{M a^2}{C} J_2 \quad (2)$$

where M is the Earth's mass and a is its mean radius. The Hamiltonian describing the rotational motion of the Earth reads (Laskar & Robutel, 1993; Neron de Surgy & Laskar, 1997):

$$\mathcal{H}(X, \psi, t) = \frac{\alpha}{2} X^2 + \sqrt{1 - X^2} (\mathcal{A}(t) \sin \psi + B(t) \cos \psi) \quad (3)$$

where the action $X = \cos \varepsilon$ (ε being the Earth's obliquity), ψ being the precession angle, the functions $\mathcal{A}(t)$ and $B(t)$ describe the evolution of the Earth's orbital plane under planetary secular perturbations, and the precession "constant" α is defined as:

$$\alpha = \frac{3H}{2\omega} \left(\frac{n_M^2 m_M}{(1 - e_M^2)^{3/2}} \left(1 - \frac{3}{2} \sin^2 i_M \right) + \frac{n_\odot^2 m_\odot}{(1 - e_\odot^2)^{3/2}} \right) \quad (4)$$

where ω is the Earth's spin rate; m_M and m_\odot are the masses of the Moon and the Sun respectively, n_M and n_\odot are their mean motions, e_M and e_\odot are their orbital eccentricities, while i_M is the orbital inclination of the Moon.

A quasi-periodic decomposition of the perturbation function $\mathcal{A}(t) + iB(t)$ into N modes of amplitudes, frequencies, and phases α_k , ν_k , and ϕ_k respectively, allows us to write the Hamiltonian as (Laskar & Robutel, 1993):

$$\mathcal{H}(X, \psi, t) = \frac{\alpha}{2} X^2 + \sqrt{1 - X^2} \sum_{k=1}^N \alpha_k \sin [\nu_k t + \phi_k + \psi]. \quad (5)$$

This is identical to the Hamiltonian of an oscillator with frequency $\alpha \cos \varepsilon_0$, perturbed by a small amplitude quasi-periodic external forcing term. A resonance is thus encountered when the Earth's precession frequency $\psi \approx \alpha \cos \varepsilon_0 = 50.47 \text{ arcsec/yr}$ is equal in magnitude and opposite in sign to one of the frequencies ν_k . In fact, the quasi-periodic decomposition of $\mathcal{A}(t) + iB(t)$ reveals that a periodic term of small amplitude, related to the contribution of Jupiter and Saturn, and namely labeled $s_6 - g_6 + g_5$, is characterized by a frequency $\nu_{23} = -50.33 \text{ arcsec/yr}$ (Laskar et al., 1993, 2004). This suggests that variations in the precession frequency ψ , propagating from variations in the dynamical ellipticity H through the precession "constant" α , can impose a rotational resonance. This scenario was examined parametrically by Laskar et al. (1993) who found that a perturbation in H of -0.223% relative to the present value suffices to encounter such a resonance, forcing a significant obliquity increase of about 0.5° (see Figure 9 of Laskar et al., 1993). To decide whether this resonance was encountered during the Cenozoic ice ages requires a full model for the Earth's spin evolution, including tidal dissipation and mantle convection, which is out of the scope of the present work. However, the position of the $s_6 - g_6 + g_5$ resonance is still a landmark to evaluate the physical implications of the Earth's deformation under the history of glacial loading we are considering here.

3. Glacial Isostatic Adjustment and the Sea Level Equation

The essential ingredients in modeling GIA are the spatio-temporal evolution of the surface loading and the rheological model of the Earth that dictates its response to that loading. We model a spherically symmetric Earth with radial density and elastic properties based on the PREM model (Dziewonski & Anderson, 1981). The core is modeled as an inviscid homogeneous fluid sheltered by the mantle that is approximated to behave viscoelastically (Wu & Peltier, 1982). A choice has to be made on the rheology between linear (Newtonian) or nonlinear, describing the stress-strain relation (Gasperini et al., 2004). We adopt the former description allowing the mantle

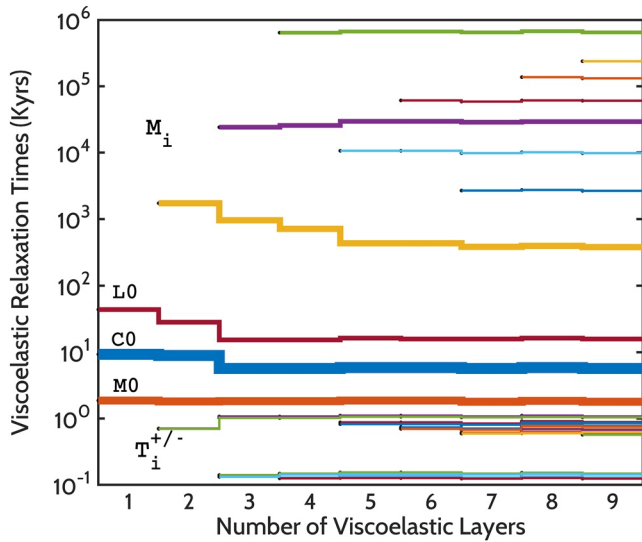


Figure 1. Viscoelastic relaxation times, $\tau_i = -1/s_i$, of harmonic degree $l = 2$ computed in the normal modes theory formalism, for an increasing stratification of the Earth's model. Zeroth modes are associated with the boundaries of the mantle with the core and the lithosphere. Buoyancy modes, M_i , and transient doublets, T_i , emerge at each added interface between viscoelastic layers, however, their contribution to the multi-exponential form (Equation 6) decays with increasing layering. The labeling of modes is based upon the shear kernels derived on the basis of a viscoelastic extension of Rayleigh's elastic variational principle (Peltier, 1976). The strength of each mode is indicated by its thickness. The partitioning of the viscoelastic layers is consistent with the detected seismological discontinuities of the PREM model.

to respond as a linear Maxwellian body, enveloped by an elastic lithosphere. The radial viscosity profile of the mantle was adopted from joint nonlinear inversions by Lau et al. (2016).

When forced at the surface, the response of the model described above is quantified by the Love numbers. Closed form solutions for these Love number are hard to obtain for a radially stratified mantle, thus the numerical normal modes theory has been adopted (Peltier, 1974, 1976, 1985). The three surface loading Love numbers: k^L , h^L , l^L associated with the gravitational perturbation, vertical, and horizontal displacements respectively take the general form:

$$x_i^L(t) = x_i^{L,e} \delta(t) + H(t) \sum_{i=1}^N x_{i,i}^L e^{s_{i,i} t} \quad (6)$$

where $x_i^{L,e}$ is the elastic loading Love number of harmonic degree l , $H(t)$ is the Heaviside step function, and $x_{i,i}^L$ are the viscoelastic residues associated with the $s_{i,i}$ normal modes corresponding to viscous relaxation times $\tau_{i,i} = -1/s_{i,i}$. The number N of these normal modes is governed by the number of discontinuities in the radial profile. Several numerical techniques are available for the computation of the Love numbers in the context of GIA, and a community benchmark study (Spada et al., 2011) tested the agreement. We followed the procedure and recipes carefully laid out in the monograph of Sabadini et al. (2016) and solved the governing system of equations describing the Earth's deformation using the propagator matrix method. We tested our code's precision against the benchmark study and we report an agreement of one part in 10^8 for the Love numbers, and one part in 10^7 for the normal modes.

Using volumetric averages of the internal properties, a choice has to be made on the number of layers for the viscoelastic mantle. In Figure 1, we summarize the variation of the relaxation times for an increasing level of stratification. The radial viscosity profile was volume averaged over the needed number of layers. As expected, the number of modes increases as we increase the number of discontinuities. The C_0 , L_0 , and M_0 modes, associated with the core-mantle and mantle-lithosphere boundaries, are of strongest viscous amplitudes and converge toward constant values for a number of layers as small as three. With each added viscoelastic interface, a buoyancy mode M_i and a transient doublet T_i^\pm emerge, though these modes feature viscous amplitudes that decay as i increases. Thus for our purposes here, we assume that a larger number of layers is not needed to capture the essential viscoelastic response of the Earth, as the modes of strongest amplitudes converge fast enough with stratification, and we proceed with a model of nine viscoelastic layers in the mantle.

After computing the Love numbers, we utilize the SLE to find the temporal evolution of the geoid, which when decomposed harmonically, allows us to compute a history of the dynamical ellipticity. The SLE constructs the self-consistent gravitational redistribution of ice and water across the surface of the Earth. Its mathematical theory and numerical implementation are undergoing continuous development by the community since its first introduction in the 1970s through a series of seminal articles (Adhikari et al., 2016; Clark et al., 1978; Farrell & Clark, 1976; Kendall et al., 2005; Milne & Mitrovia, 1998; Mitrovia & Milne, 2003; Peltier, 1974, 2015; Peltier & Andrews, 1976; Spada & Stocchi, 2007).

The implicit nature of the SLE being a three dimensional nonlinear integral equation, in the form of a Fredholm equation of the second kind, calls for an iterative approach in order to be solved. We adopt the theory and numerical code developed over the past two decades and called SELEN⁴ (Sea IEVeL EquationN solver, version 4.0; Spada & Melini, 2015, 2019; Spada et al., 2012; Spada & Stocchi, 2007). In SELEN⁴, the SLE is solved by a pseudo-spectral iterative approach (Mitrovia & Peltier, 1991) over a spatially discretized Earth surface on a spherical grid of icosahedron shaped pixels (Tegmark, 1996). The gravitationally self-consistent surface loading is computed allowing for shoreline migration and the transfer of ice between grounded and marine-based.

The implicit nature of the SLE being a three dimensional nonlinear integral equation, in the form of a Fredholm equation of the second kind, calls for an iterative approach in order to be solved. We adopt the theory and numerical code developed over the past two decades and called SELEN⁴ (Sea IEVeL EquationN solver, version 4.0; Spada & Melini, 2015, 2019; Spada et al., 2012; Spada & Stocchi, 2007). In SELEN⁴, the SLE is solved by a pseudo-spectral iterative approach (Mitrovia & Peltier, 1991) over a spatially discretized Earth surface on a spherical grid of icosahedron shaped pixels (Tegmark, 1996). The gravitationally self-consistent surface loading is computed allowing for shoreline migration and the transfer of ice between grounded and marine-based.

SELEN⁴ also accounts for the influence of the rotational feedback on sea level. For a more elaborate explanation on the SELEN⁴ scheme, the reader is referred to the supplementary material of Spada and Melini (2019).

In almost all numerical implementations of the SLE, continuous solutions in time have not been used, and a time discretization for all quantities is imposed over a piece-wise function ($n = 1..N$). With this time discretization and the pseudo-spectral approach, the geoid response function, expanded in spherical harmonics of degree l and order m , is written as:

$$\mathcal{G}_{lm} = \frac{3}{\rho^E} \sum_n^N \frac{\Delta \mathcal{L}_{lm,n}}{2l+1} \left(1 + k_l^L + \sum_{i=1}^M \frac{k_{l,i}^L}{s_{l,i}} \left(e^{s_{l,i}(t-t_n)} - 1 \right) \right) H(t-t_n) \quad (7)$$

where $\Delta \mathcal{L}_{lm,n} = \mathcal{L}_{lm,n+1} - \mathcal{L}_{lm,n}$, with $\mathcal{L}_{lm,n}$ representing the harmonic decomposition and temporal discretization of the surface loading function \mathcal{L} , and ρ^E being the average density of the Earth. Finding the variation in the geoid allows us to compute the variation in the geopotential Φ using the classical Bruns formula (Heiskanen, 1967):

$$\mathcal{G} = \frac{\Phi}{g}. \quad (8)$$

With the harmonic decomposition of the geoid variation, and the multipolar expansion of the geopotential into the well known Stokes' coefficients c_{lm} and s_{lm} (Yoder, 1995), one can write the gravitational zonal harmonics of the Earth as (Mitrovica & Peltier, 1989):

$$\delta J_l(t) = -\frac{1}{a} \sqrt{2l+1} \mathcal{G}_{l0}(t) = -\frac{1}{a} \sqrt{2l+1} \delta c_{l0}(t) \quad (9)$$

Hence the variation of the dynamical ellipticity (Equation 2) relative to its present day value $H_0 \approx 3.27 \times 10^{-3}$ (Burša et al., 2008) can be written as:

$$\frac{\delta H(t)}{H_0} = \frac{\delta J_2(t)}{H_0 \mathcal{K}} \left(1 - \frac{2}{3} H_0 \right) \approx \frac{\delta J_2(t)}{H_0 \mathcal{K}} = -\frac{\sqrt{5}}{H_0 \mathcal{K} a} \delta c_{20}(t) \quad (10)$$

where $\mathcal{K} = \frac{C}{Ma^2}$ is the so-called structure constant. Thus the problem of finding the relative variations in the dynamical ellipticity reduces for us to finding the geoid response function \mathcal{G} in the framework of the SLE solver. Another contribution arises from variations in the centrifugal potential, but we ignore that based on the arguments in Appendix A.

4. Cenozoic Ice History

In addition to the Earth model, an ice loading history is required for the SLE solver to predict the evolution of the dynamical ellipticity with time. We use the most common proxy of benthic foraminiferal measurements of oxygen isotopes ratio to constrain the global ice volume (Shackleton, 1975; Zachos et al., 2008). The latter is known to have contributions from both ice volumes and water temperature, nevertheless Mg/Ca benthic foraminiferal ratios have recently been used as an independent proxy for deep ocean temperature (Cramer et al., 2011; Lear et al., 2000; Sossian & Rosenthal, 2009). The separation of the contributions is established via a paleotemperature equation (Lynch-Stieglitz et al., 1999; O'Neil et al., 1969). The ice contribution is then scaled into a variation in global mean sea level (GMSL) using a certain calibration (see Gasson, DeConto, & Pollard, 2016; Winnick & Caves, 2015 for discussions on uncertainties associated with a chosen calibration). This sea level equivalence of ice is then scaled to a percentage of present ice volume. Based on this technique, we adopt the oxygen isotope splice and its associated sea level equivalent of ice compiled recently in Miller et al. (2020), covering the Cenozoic era, starting 66 Ma (we use the usual convention in stratigraphy where ka, Ma (thousand, million years) denote dates in the past from now, while kyr, Myr denote durations). This compiled splice, denoted M20 hereafter, is similar to that in De Vleeschouwer et al. (2017), but is composed entirely of Pacific records, minimizing the effects of temperature and salinity present in other regions due to deep circulation changes. That said, uncertainties of the glaciation history we shall derive from the oxygen isotopic record mainly propagate from three different sources: uncertainties on the oxygen isotope record itself, uncertainties associated with filtering out the temperature contribution to the record, and uncertainties associated with the conversion of the remaining

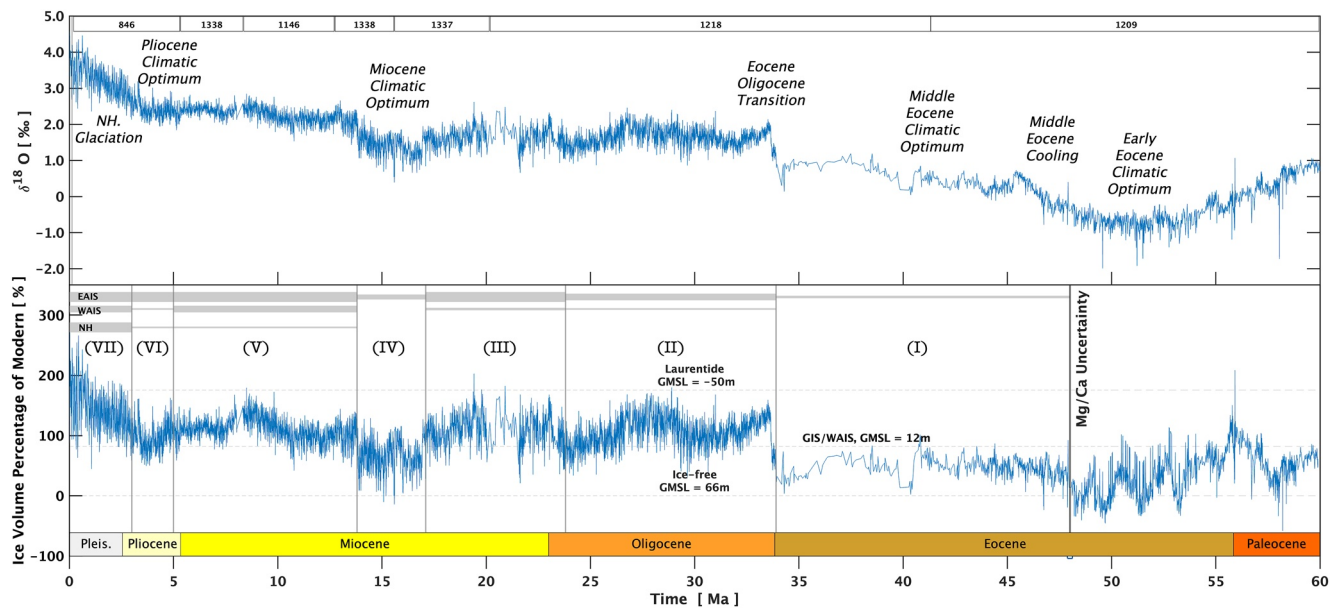


Figure 2. Cenozoic benthic foraminiferal $\delta^{18}\text{O}$ records from the splice compiled in (Miller et al., 2020) [M20], and their ice volume contribution after the removal of the temperature contribution à la Cramer et al. (2011). The first panel is the isotope variation with time relative to the VPDB standard; the drilling sites are indicated on the top of the panel. The second panel is the ice variation with time in volume units on the right axis and in percentage relative to modern values on the left axis. The ice free line is equivalent to 66 m of sea level increase above present, corresponding to the total increase in sea level if the Earth becomes ice free. The GIS/WAIS (Greenland and West Antarctic Ice Sheets) and the Laurentide lines are equivalent to 12 and -50 m sea level variations. The gray bars on top of the second panel are rough sketches of the glacial evolution of the ice sheets across eight intervals that we have defined for the spatio-temporal glacial function used in our simulations (more on that in Section 5). The 8th interval covers the last glacial cycle.

pure glacial component to GMSL variations and eventually absolute ice volume (the calibration used in the M20 splice is $0.13\text{‰}/10\text{m}$). These uncertainties are collectively quantified in Section 5.

The M20 splice, Figure 2, is interpreted to distinguish between a mostly unglaciated Cenozoic Hothouse with $\delta^{18}\text{O} < -0.5\text{‰}$, a moderate WarmHouse having ephemeral ice sheets with $-0.5 < \delta^{18}\text{O} < 1.8\text{‰}$, and an Icehouse with continental scale ice sheets on one or both of the Earth's poles with higher isotopic values (Huber et al., 2018; Miller et al., 1987; the terms Hothouse, WarmHouse, and Icehouse have been adopted from Westerhold et al., 2020). A long term warming stage started in the late Paleocene (60–54 Ma) and led to the Paleocene-Eocene thermal maximum followed by a stable interval of minimum isotopic values during the Early Eocene climatic optimum (55–48 Ma). The middle Eocene after that witnessed a cooling phase with an increase in $\delta^{18}\text{O}$ around 2‰ , then the climate relatively stabilizes until the end of the Eocene with $\delta^{18}\text{O} \approx 1\text{‰}$. Thus during the Eocene, the Earth was largely ice-free, with only partial glaciation on the highly elevated plateaus of the eastern part of Antarctica (Rose et al., 2013), and the south-eastern part of Greenland (Eldrett et al., 2007; Tripathi & Darby, 2018). High amplitude ice volume oscillations are thus most probably due to the error in the Mg/Ca record. This limitation is discussed in details in Cramer et al. (2011), putting much larger errors on the record before 48 Ma, which explains the negative ice volumes obtained before this period. As such, we have limited our model prediction of the evolution of the dynamical ellipticity to the interval covering the last 47 Myr (Section 5). The relatively stable final phase of the Eocene was terminated by one of the major known Myr-scale features of the Cenozoic, the Eocene-Oligocene transition (EOT) around 34 Ma (Coxall et al., 2005), which is associated with the rapid glaciation of the Antarctic ice sheet (AIS) up to a continental scale, marking the onset of the Earth's Icehouse.

Following the EOT, the AIS was almost only established on the Eastern terrestrial region (EAIS; Galeotti et al., 2016). Based on the M20 splice, its evolution during the Oligocene shows that it was not yet permanently developed (Figure 2), as we have large scale oscillations that peaked at the loss of more than 60% of the AIS after the EOT around 30 Ma, indicating its long term instability. The extent to which the West Antarctic Ice Sheet (WAIS) participated in the mostly unipolar Oligocene glaciation is largely unknown.

During the Early to mid-Miocene, major variations occurred in the AIS volume and extent. The M20 splice estimates larger variations than those proposed by Pekar and DeConto (2006) 50%–125% of modern EAIS values). General circulation models previously failed to completely simulate such large scale variations because of strong hysteresis effects and the glacial-interglacial symmetry (Gasson, DeConto, Pollard, & Levy, 2016; Liebrand et al., 2017). Moreover, after continental scale glaciation is achieved, the resultant ice sheet is rather stable in the simulations (Langebroek et al., 2009; Pollard & DeConto, 2005). Modeling this variability probably requires adding more atmospheric components to account for ice sheet-climate feedback (Gasson, DeConto, Pollard, & Levy, 2016), or incorporating mechanisms such as hydro-fracturing and ice-cliff instabilities (Pollard et al., 2015). These large oscillations were punctuated by the Miocene Climatic Optimum (17–13.8 Ma). The latter was a period of reduced ice volume where near ice free conditions were attained around 15 Ma, probably establishing the most recent ice-free Earth.

Following this warm period, the Middle Miocene Climatic Transition involved three major steps of cooling and consequently sea level falls resulting in a permanent EAIS (Miller et al., 2020) and a global ice volume higher than today (~120%). The ice volume then remained approximately constant until early Pliocene. This scenario of Antarctic stability for the past 8 Myr is also supported by cosmogenic isotope data from the Ross Sea (Shakun et al., 2018). During the last 3 Myr, frequent build-ups of ice volume associated with sea level drops around 110 m below present were encountered, indicating the onset of continental scale Northern Hemispheric ice sheets (DeConto et al., 2008; Shackleton et al., 1984). The largest of these build-ups were during the past 800 Kyr (the Last Glacial Maximum [21 ~ 26 ka] was associated with a sea level drop ~130 m [Austermann et al., 2013]).

5. Evolution of Dynamical Ellipticity

In the framework of the SLE solver, the ice volume input should be temporally discretized as we discussed (in the simulations that follow, we use a temporal resolution of 1 kyr), but also spatially distributed over the surface of the Earth. Since an exact distribution is currently impossible to obtain over such a prolonged history, we approximate the input by conserving the global limit from the M20 splice (Figure 2), and further abiding by major known glacial events and the available geological constraints that help model the glacial spatial distribution. The latter are summarized in Table 1, and we use them to create a spatio-temporal glacial history of eight intervals: the pre-EOT interval, the Oligocene, the Early Miocene until the Middle Miocene Climatic Optimum (MMCO), the warm period of the MMCO, a post-MMCO interval until the Pliocene Climatic Optimum, the Pliocene Climatic Optimum, the last 3 Ma until the last glacial cycle, and the last glacial cycle (Figure 2). The geological evidence compiled in Table 1 allows us to specify the regions of possible glaciation within each interval. After these regions are specified, the global ice volume is distributed among these regions by following the proportions from the ICE-6G model (Peltier et al., 2015). We elaborate in detail on this distribution procedure in Appendix B. Such a distribution may not be adequate for high precision geodetic calculations. However, we are after the second degree harmonic decomposition of the load, which is characterized by even parity and symmetry under rotation. Also, the change in oblateness reflects long wavelength deformation, so abiding by major climatic events, it is safe to assume that we are capturing the backbone of the evolution of the dynamical ellipticity. Our sensitivity tests will later show that variations in the spatial distribution are only higher order corrections.

Using SELEN⁴, we discretize the Earth's surface onto a Tegmark grid of equal-area icosahedron-shaped pixels (Tegmark, 1996). The grid is characterized by a resolution parameter R that yields a number of pixels $P = 40R(R - 1) + 12$. In our suite of simulations, we set $R = 30$, which gives $P = 34,812$. The SLE is solved over two nested loops, and the convergence of the solution as a function of the number of iterations is discussed in Milne and Mitrovica (1998) and Spada and Melini (2019). Based on the convergence tests in these studies, all of our simulations were performed over three internal and three external loops. We use the 11-layers Earth's model (9 viscoelastic mantle layers, along with the core and the elastic lithosphere) described earlier, and we provide SELEN⁴ with the needed Green's functions based on the viscoelastic response of this model.

Global ice input uncertainty propagates from the uncertainty of the sea level variation. Estimates of uncertainty on the latter vary between ± 10 and ± 20 m (Kominz et al., 2008; Miller et al., 2012; Raymo et al., 2018). Thus we consider these limits as 1σ and 2σ error estimates respectively, and we consequently create a white Gaussian noise with these amplitudes to perform 40 simulations of the SLE solver. In addition to this error, sea level variation is under a systematic uncertainty propagating from the variation in the volume of the oceans basins and a

Table 1

A Compilation of References Used to Constrain the Spatio-Temporal Distribution of Ice Over the Earth's Surface

Geologic evidence/geographic constraint	Study type	Reference
• Partial glaciation in Antarctic high elevation regions during the Early Eocene.	GE	Rose et al. (2013)
• Antarctic expansion into marine terminating glaciers, specifically around the Aurora subglacial basin.	GE	Gulick et al. (2017)
• Simulating the inception of the EAIS requires small ice caps on elevated plateaus.	S	DeConto and Pollard (2003)
• Sediment rafting by glacial ice on the S-E end of Greenland dating back late Eocene.	GE	Eldrett et al. (2007)
• Middle Eocene episodic glaciation on Greenland from ice-rafted Fe-oxide grains.	GE	Tripati and Darby (2018)
• Seismic stratigraphic evidence for ice in the Ross Sea during Oligocene-Miocene.	GE	Bart (2003) and Bartek et al. (1992)
• Oligocene grounded ice in the WAIS around and far from Marie Byrd Land.	GE	Rocchi et al. (2006) and Sorlien et al. (2007)
• Terrestrial retreat of the EAIS during the Miocene Climatic Optimum.	GE	Levy et al. (2016)
• Expansion of terrestrial ice across the Ross Sea continental shelf around 24.5–24 Ma.	GE	Hauptvogel et al. (2017)
• Terrestrial AIS stability for the past 8 Ma from cosmogenic isotope data.	GE	Shakun et al. (2018)
• Early Pliocene loss of ice from WAIS and Greenland.	GE	Naish et al. (2009)
• Substantial marine ice retreat in the EAIS during Early Pliocene.	GE	Cook et al. (2013)
• Simulating the AIS evolution over the last 3 Myr: Separation between polar caps' contributions to the global volume.	S	Pollard and DeConto (2009)

Note. Some elements of the list correspond to geological evidence of various ice sheets extent over the Cenozoic (indicated by GE). Others correspond to modeling of ice sheets, specifically used to simulate onsets of continental glaciation (indicated by S).

contribution from tectonic changes (Conrad, 2013). Constraining the former was already done in the M20 data set based on Cramer et al. (2011) by limiting the ice contribution to the sea level variation through end member scenarios. To remove the tectonic contribution, we apply a LOESS regression filter (a generalized moving polynomial regression; Cleveland & Devlin, 1988), with a window of 20 Myr, to isolate and then remove variability occurring over plate tectonic timescales, and then keeping only short timescale variability that is most likely due to the ice volume contribution.

In Figure 3, we plot in red the evolution of the relative perturbation in dynamical ellipticity based on our SLE solutions. In black are solutions with 1σ correction, and 2σ solutions are in gray. Since the present Earth is in an interglacial period, the mean of the perturbation across the Cenozoic is negative, as glaciation involves a net transfer of mass into the poles, reducing the dynamical ellipticity. As discussed earlier, the viscoelastic response attempts to compensate for this reduction by increasing the flattening again, but the overall perturbation nonetheless remains negative. The mean of the oscillations over the Eocene approaches zero, with relatively high amplitude oscillations attributable to the poor constraint of the Mg/Ca ratios.

The first major amplification in our model prediction of the perturbation occurs in a step-function like jump and is, as expected, across the EOT (34 Ma), upon the initiation of a continental scale glaciation on Antarctica. After that, the evolution of the terrestrial East Antarctic Ice sheet results in moderate amplitude oscillations averaging around -0.04% (Figure 3). The following major Myr-scale variation in the secular trend occurs around the Miocene climatic optimum when the Earth enters a period of reduced glaciation reaching near ice-free conditions. During this period, the relative perturbation in the ellipticity trend drops to around -0.012% , then attains its global average again with the initiation of a larger scale glaciation on West Antarctica and Greenland, and with the stabilization of the EAIS. The final major variation in the trend occurs when the Earth transitions into its bipolar glaciation. During the last 3 Myr, the dynamical ellipticity enters a regime of extremely high amplitude oscillations that are maximized during the last million years. The average value during this period drops to around -0.05% (second panel of Figure 3), and reaches -0.07% during the most recent glacial cycles. Glacial peaks over the same period average around -0.11% , and reach -0.17% within the 2σ envelope. The last interglacial period is marked with a global maximum with an average relative perturbation of $+0.08\%$. We note that using simpler

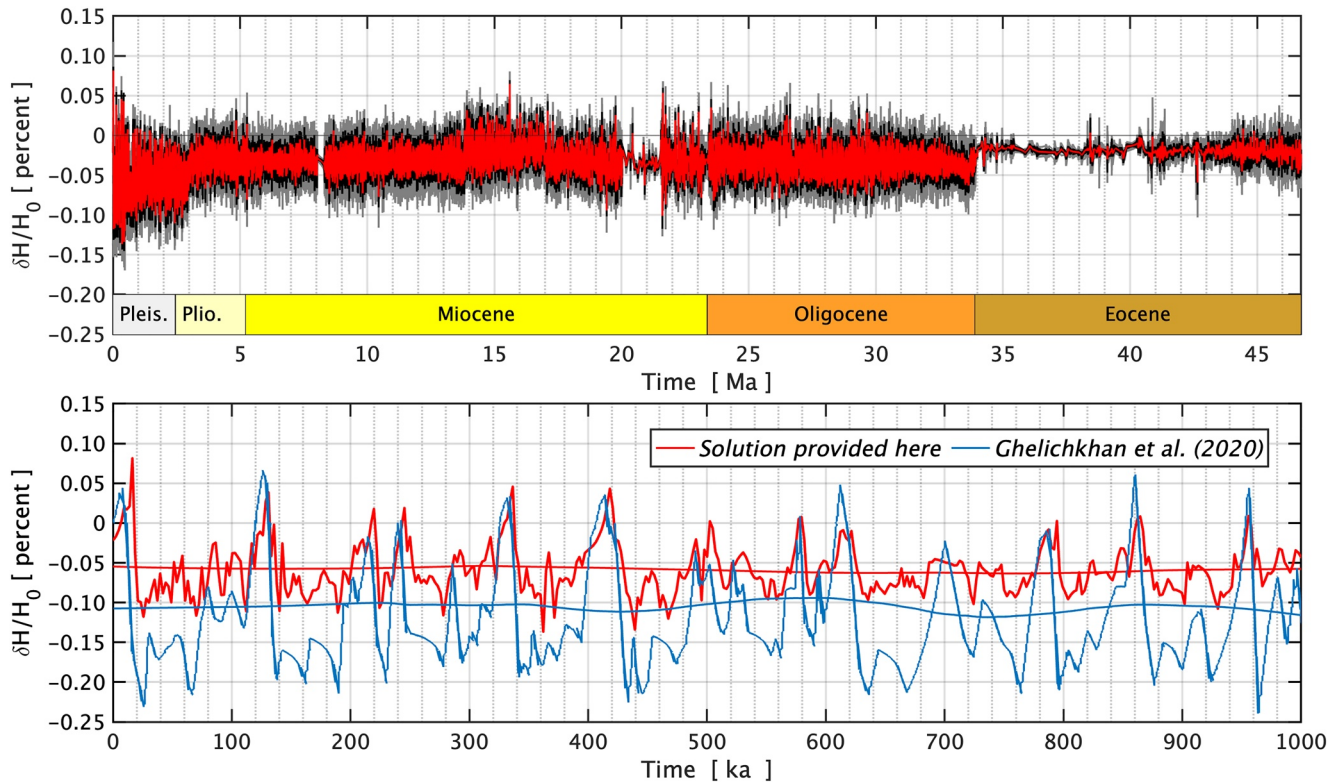


Figure 3. Model prediction of the evolution of the relative perturbation in dynamical ellipticity due to glacial isostatic adjustment (GIA) over the past 47 Myr (the limit beyond which Mg/Ca data is compromised by large errors). *Top:* Evolution in red corresponds to the ice load variation derived from the M20 $\delta^{18}\text{O}$ splice of Figure 2 and internal profiles of the Earth's structure averaged from the PREM model with viscosity variation adopted from Lau et al. (2016). In black and gray are 40 other simulations accounting for 1σ and 2σ uncertainty in ice as discussed in the text. *Bottom:* A smaller window over the past million years only. Plotted is our solution compared to that provided in Ghelichkhan et al. (2020), each with their smoothed secular trends.

geometries of glacial spread yields results that are well confined within this uncertainty envelope. For instance, replacing the spatial evolution of the Antarctic glacial distribution by the spread of the Last Glacial Maximum (LGM), which almost represents a spherical cap confined within a circle of latitude at -66° , yields an evolution of the dynamical ellipticity within the 2σ uncertainty envelope for the Eocene and parts of the Miocene, and within 1σ for the rest of the Cenozoic.

In a similar procedure to that adopted here, Ghelichkhan et al. (2020) also derived the evolution of the dynamical flattening due to GIA over the last 3 Myr. In the second panel of Figure 3, we compare their solution to the present work over the past million years only. By visual inspection, the two solutions appear to evolve in-phase along the glacial cycles within the same order of magnitude. We also investigated the periodicity of both solutions and they matched identically. However, the evolution in Ghelichkhan et al. (2020) involves more amplified oscillations and a larger secular reduction in the dynamical ellipticity. In fact, the plotted secular trends show that our estimate is around half that produced in their analysis (around -0.055% compared to -0.11%). Their study adopts an ice history from Raymo et al. (2011), which is also developed from foraminiferal oxygen data. However, it is not clear whether their direct scaling took into account the contribution of temperature or not, so that could partially justify the discrepancy. However, as our ice sensitivity envelope well constrains the long term trend, we expect the difference to have emerged from adopting different viscosity profiles for the Earth, thus we perform a viscosity sensitivity analysis in Section 5.2.

5.1. Pacing by Astronomical Beats

On timescales of $10^1 \sim 10^3$ kyr, the climatic state behaves as a nonlinear system that responds to quasi-periodic astronomical tuning. To better understand this modulation and its influence on the dynamical ellipticity variation, we perform in Figure 4 a continuous wavelet transform (CWT) using MATLAB for both the ice input data and our

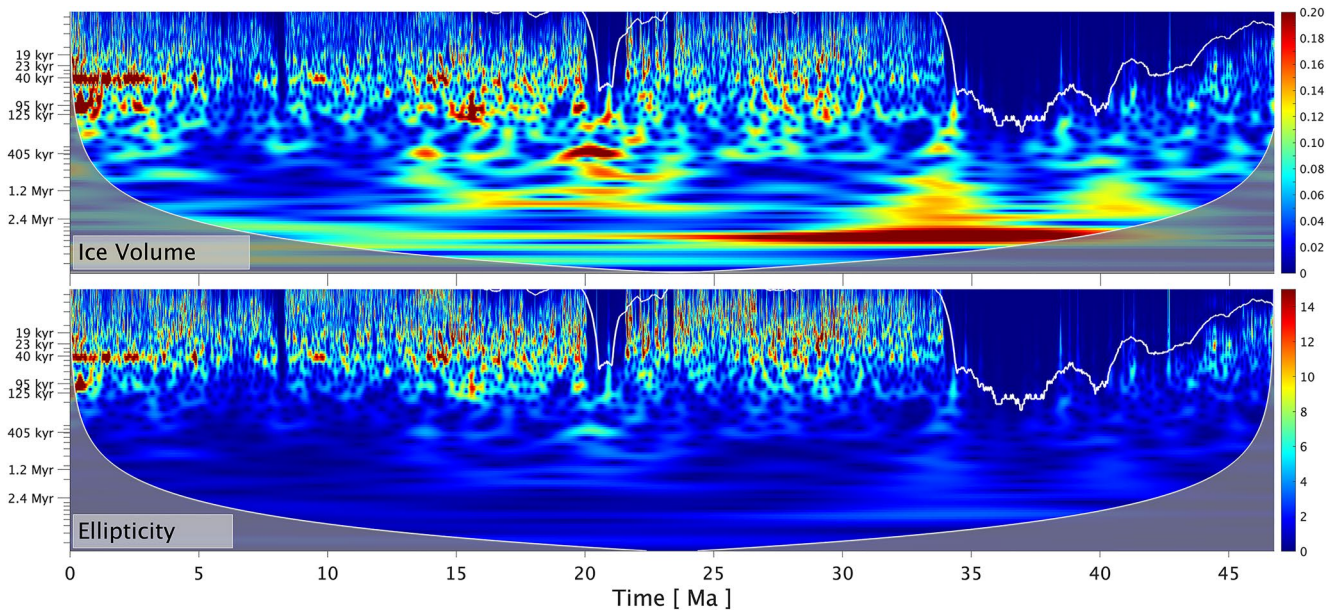


Figure 4. Continuous Wavelet Transforms (CWT) performed for the ice volume input provided to our simulations and the computed dynamical ellipticity evolution. The color mapping shows the relative power of varying amplitudes of spectral components of the data. Major spectral components associated with orbital forcing are identified on the y-axis. On top of the scalogram, the top white curve corresponds to the computed local Nyquist frequency. The bottom shaded area represents the cone of influence, which is the area potentially affected by edge-effect artifacts, and is suspected to have time-frequency misinformation.

dynamical ellipticity evolution solution. That of the former is similar to that present in Miller et al. (2020), and on a Myr timescale, it shows the general transition in the power spectrum from a climate that was mostly dominated by long period orbital forcing, into a regime of short period forcing dominance. The long eccentricity and obliquity cycles are clearly present before the EOT, along with a less prominent shorter eccentricity (405 kyr) modulation. The long periodicity dominance continued across the Oligocene, where large amplitude oscillations in ice volume were paced by the long obliquity cycle, along with an emerging dominance of the eccentricity period modulation (Boulila et al., 2011). During this period, we also identify the short eccentricity (100 kyr) and obliquity (40 kyr) bands being present to a lesser power (Liebrand et al., 2017; Pälke et al., 2006).

Across the Miocene, the attenuation of the long period orbital forcing control is clear, in favor of a growing effect for the 405 kyr eccentricity and 40 kyr obliquity cycles. The emergence of the short obliquity forcing modulation is justified in Levy et al. (2016) by the expansion of ice sheet margins into marine environments, which is a persistent feature after the Miocene Climatic Transition, 15 Ma. During the last 3 Myr, blow-ups of ice volume were associated with extreme sea level falls and the onset of a continental scale Northern Hemispheric ice sheets. The 40-kyr obliquity cycle continued to be dominant with the 100 kyr eccentricity cycle which takes over across the last 800 kyr, although it was already present before this transition. We note the clear attenuation of the 405 kyr eccentricity cycle that was dominant during intervals of the Miocene, and the almost complete muting of the long eccentricity and obliquity cycles. This general trend was also identified in another compiled oxygen splice (Westerhold et al., 2020), explained by the spectrum of different nonlinear responses of the climate system to orbital forcing during different climate states: Eccentricity cycles should dominate the pacing of the Hothouse and the WarmHouse, as the eccentricity dominates temperature responses in low latitudes, while obliquity cycles dominate over the CoolHouse and the IceHouse, as high latitude glaciation is mostly influenced by the obliquity. This feature is also clear in our spectral analysis, except for the fact that long term obliquity pacing was also prominent even before the Oligocene.

As for our dynamical ellipticity evolution, its CWT is a filtered version of that of the ice input. Since its evolution is dictated by the evolution of the surface loading, one can expect to have an identical pacing for both signals. However, the solid Earth's response behavior is orchestrated by the relaxation spectrum of the normal modes whose timescales range between 10^{-1} and 10^5 kyr (Figure 1). We also note that the modes with the longest relaxation times correspond to buoyancy modes with very low normalized viscous amplitudes $k_{2,i}^L/s_{2,i}$, and thus

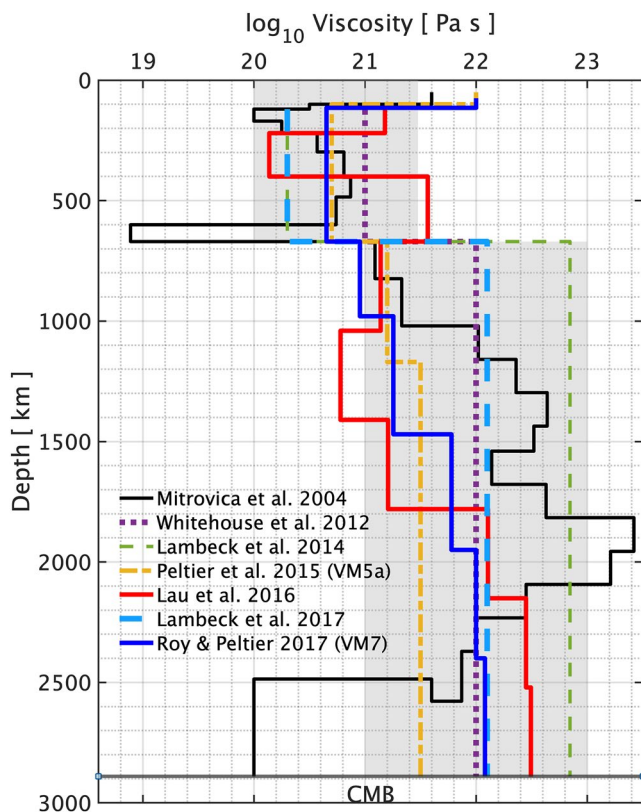


Figure 5. Mantle radial viscosity profiles from different models in the literature (Lambeck et al., 2017, 2014; Lau et al., 2016; Mitrovia & Forte, 2004; Peltier et al., 2015; Roy & Peltier, 2017; Whitehouse et al., 2012). Most models are inferred from inversions of glacial isostatic adjustment (GIA) observables including sea level variations, rebound, rate of change of the second zonal harmonic, and polar wander. Almost all models involve at least an order of magnitude viscosity transition between the mean of the upper mantle and the mean of the lower mantle, though some models advocate a more acute viscosity transitions across the 660 km discontinuity. Such high viscosity contrast models do not reconcile present observations of the true polar wander and the rate of change of J_2 (Argus et al., 2021). Shaded are the areas we cover in our viscosity sensitivity analysis.

lower mantle to a mean value in excess of 10^{22} Pa s. This low contrast viscosity model of Lau et al. (2016) is very similar to the VM7 model of Roy and Peltier (2017) and the VM5a of Peltier et al. (2015), especially in the upper part of the lower mantle. In contrast, the profile used in Ghelichkhan et al. (2020) is the high viscosity contrast model of Mitrovia and Forte (2004) (further updated in Forte et al., 2009; Moucha et al., 2008 removing the soft layer at the 660 km discontinuity). Although this model was derived from joint inversions of mantle convection and GIA constraints, it was later shown that it overestimates solid Earth relaxation times inferred from shoreline displacement histories in the James Bay area (Pendea et al., 2010; Roy & Peltier, 2015). Models inferring more pronounced contrast across the seismic discontinuity are completely ruled out by the present true polar wander constraints and global positioning system observations of the crustal vertical motion over the North American continent (Argus et al., 2021).

We proceed by performing a systematic exploration of the dynamical ellipticity solution's sensitivity to mantle viscosity variations. We perform simulations for effective viscosity values, namely a single value for the upper mantle and another single value for the lower mantle. For the specified models with more layering, volumetric averaging was performed over concentric spherical shells. As previously predicted by Mitrovia and Forte (1995), the results are mostly insensitive to viscosity variations in the upper mantle and almost entirely dependent on the

minimal contribution to the summation in Equation 7. Hence the viscous relaxation of the solid Earth acts as a high pass filter that will only keep short periodicities at play. Thus the CWT of the dynamical ellipticity attenuates the imprints of long orbital forcing, and maintains the pacing by the short obliquity and eccentricity cycles. It must be stressed that this frequency filter is only associated with the physics under study. A complete study of solid Earth deformation would incorporate low frequency signals associated with mechanisms like mantle convection and plate tectonics.

5.2. Viscosity Profiles Sensitivity Test

To better constrain the evolution of the dynamical ellipticity, we investigate the effect of mantle viscosity on the presented solution. The literature is very dense with modeled profiles, and we present a sample of them in Figure 5. The problem of inferring this radial profile from GIA observables dates back to Daly (1925). In general, relative sea level histories and postglacial rebound data, specifically those from Fennoscandia or Antarctica (Mitrovia & Peltier, 1993), constrain the upper mantle's viscosity, while postglacial signals from Canada are used to constrain the upper part of the lower mantle (Peltier, 2004). Other geophysical observables, including the rate of change of J_2 and the polar wander are used to constrain the viscosity of the rest of the lower mantle (Lau et al., 2016), though these constraints may be challenged (Adhikari et al., 2018; Nakada et al., 2015). Other radial profiles were derived from joint inversion of data that include these GIA effects along with data related to mantle convection (Mitrovia & Forte, 1997, 2004; Moucha et al., 2008). Based on that, a community consensus has been established that the viscosity's radial profile increases along the Earth's depth. However, some models infer a viscosity jump of two orders of magnitude (Lambeck et al., 2014; Nakada et al., 2015) across the 660 km discontinuity, while others advocate a less acute transition (e.g., the VM7 model [Roy & Peltier, 2017]).

While these different profiles appear to be irreconcilable, those that predict high viscosity contrast between the upper and the lower mantle do not satisfy the totality of the observational constraints. The low contrast viscosity profile we have used so far is presented in Lau et al. (2016), and was constructed by analyzing GIA data using a combination of forward predictions and inversions based on nonlinear Bayesian inference. The result is constraining the upper mantle viscosity to around 3×10^{20} Pa s, the depth in between the mid-upper mantle and mid-lower mantle to around 10^{21} Pa s, and the bottom half of the

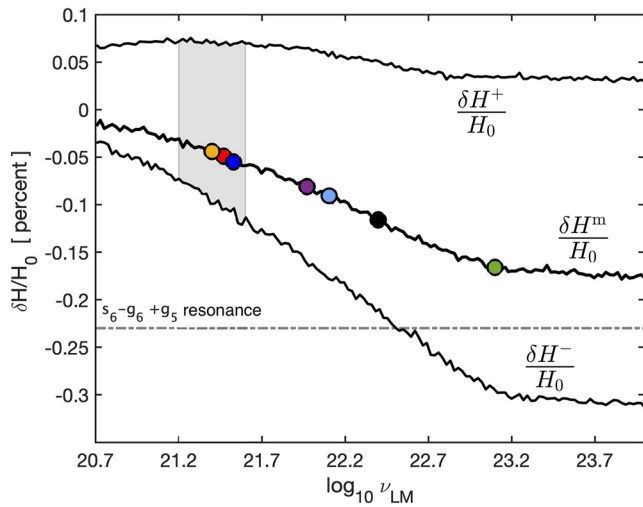


Figure 6. Relative perturbation in dynamical ellipticity over the past 3 Myr as a function of the lower mantle viscosity ν_{LM} . The upper mantle viscosity is fixed at $\nu_{UM} = 0.5 \times 10^{21}$ Pa s. The middle branch, $\delta H^m/H_0$, represents the mean of the evolution, while the upper and lower branches represent the highest and lowest peaks in the evolution, denoted by $\delta H^+/H_0$ and $\delta H^-/H_0$ respectively. For each value of ν_{LM} we perform 20 simulations that differ in the ice input to account for a random uncertainty in the interval $[0, 2\sigma]$ as discussed in the text. Each point on the branches is thus the average of these simulations. Specified points on the branch refer to the specific viscosity profiles in Figure 5 using the same color coding. The shaded area refers to a part of the identified region \mathcal{R}_1 after constraining the lower mantle viscosity to $\log_{10} \nu_{LM} \in [21.2, 21.6]$ by observed values of \dot{J}_2 (see text). We also marked the threshold value of $\delta H/H_0$, which if attained, the Earth could have crossed the $s_6 - g_6 + g_5$ resonance described in Section 2.

lower mantle. The contribution of the upper mantle is expected to arise for higher order harmonics. Thus in Figure 6, we show the results of a suite of simulations for a span of lower mantle effective viscosity ν_{LM} for fixed upper mantle effective viscosity $\nu_{UM} = 0.5 \times 10^{21}$ Pa s. Considering a time interval covering the most recent 3 Myr, we plot the mean ($\delta H^m/H_0$), the upper envelope ($\delta H^+/H_0$), and the lower envelope ($\delta H^-/H_0$) values for the evolution of our model predictions of the relative perturbation for each viscosity value. Each point on each branch is the average of 20 simulations that covered the ice uncertainty envelope. The negative values of $\delta H^m/H_0$ and $\delta H^-/H_0$ get more negative as the viscosity contrast between the upper and lower mantle increases. However, the slope of this monotonic trend is smaller for smaller values of ν_{LM} than it is for larger values. In contrast, $\delta H^+/H_0$ is less sensitive to viscosity variations. The time evolution of each simulation also shows that the difference between the long term trends grows in time, and this has two causes: the general feature of ice volume increase with time, and the accumulation of the nonlinear effects due to the solid Earth's relaxation response.

Besides the reduction in the mean, Figure 6 shows that larger values of lower mantle viscosity, corresponding to a larger viscosity jump across the 660 km discontinuity, are associated with a broader separation between the peaks, $(\delta H^+ - \delta H^-)/H_0$. This behavior of the cycles' amplitudes, along with that of $\delta H^m/H_0$, is understandable when increasing the viscosity. The latter results in an increase in the relaxation times, which reduces the value of the fluid Love number, and consequently the magnitude of the viscoelastic compensation effect. The larger the viscosity value, the more we approach the limit of elastic compensation only, which is characterized by a larger relative perturbation in the geoid and in the dynamical ellipticity. This justifies the plateau that we reach for $\log_{10} \nu_{LM} > 23.2$ Pa s. In contrast, decreasing the viscosity results in decreasing the relaxation times and increasing the viscoelastic compensation effect, thus shrinking the relative perturbation. Accounting for this viscosity effect explains the difference we obtain with the larger amplitude oscillations

in Ghelichkhan et al. (2020). The authors use the viscosity profile of Mitrovia and Forte (2004), characterized by a larger lower mantle viscosity than our volume averaged profile from Lau et al. (2016). The offset between the two solutions in Figure 3 is now clear in Figure 6, where the black dot of the former profile corresponds to $\delta H^m/H_0 = -0.116\%$, while the red of the latter profile corresponds to $\delta H^m/H_0 = -0.05\%$.

Investigating the possibility of the past occurrence of the resonance scenario discussed in Section 2, we also mark in Figure 6 the threshold value required to cross the $s_6 - g_6 + g_5$ resonance as calculated by Laskar et al. (1993). It is evident that the average value of the ellipticity variation does not cross this threshold, as it plateaus for large values of ν_{LM} as explained above. Values of $\delta H^-/H_0$, plotted on the lower curve, only cross the threshold value when $\log_{10} \nu_{LM} > 22.6$ Pa s that is, for lower mantle viscosity values excluded by the observational constraints (Argus et al., 2021), as we will further confirm in the following section.

5.3. Constraining by \dot{J}_2

The average and the amplitude of the ellipticity perturbation cycles are highly sensitive to the chosen viscosity profile. The presented solution in Figure 3 is based on a recent inference of the viscosity profile. To justify this choice in the context of our viscosity sensitivity study, we attempt to constrain our effective viscosity freedom by the observed values of \dot{J}_2 , which as discussed earlier, is the major constraint used for lower mantle viscosity (Peltier, 1983). The first Satellite Laser Ranging (SLR) based estimate of the variation of J_2 was reported in (Yoder et al., 1983) as a linear trend of $-3 \times 10^{-11} \text{ yr}^{-1}$. As time proceeded, further analysis of SLR data over longer time spans and using more satellites provided more estimates of the secular trend. In Figure 7, we compiled an inter-study comparison of this trend from different references. All studies until the late 1990s approximated the trend by a negative linear drift that is most likely an outcome of GIA (Cheng et al., 1989; Peltier, 1983; Yoder et al., 1983). However, analyses of the time span after 1995 showed a systematic decrease in this trend

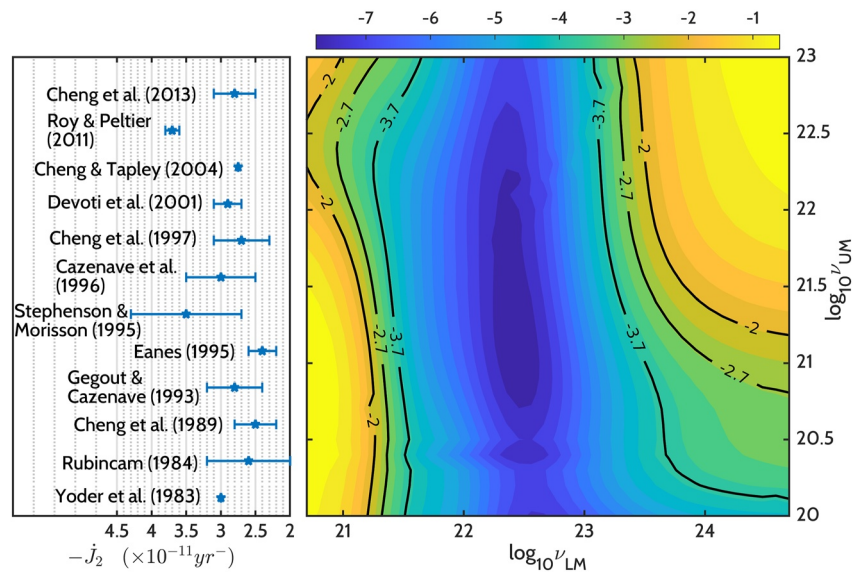


Figure 7. Constraining the choice of the viscosity profile by a comparison with observational estimates of \dot{J}_2 . Left: an inter-study of computed values of the secular trend. We note that more recent analyses were based on larger time spans of Satellite Laser Ranging (SLR) measurements and more satellites. In studies that showed the quadratic form of the variation, we only took the negative linear trend that is most likely attributed to the postglacial rebound (Roy & Peltier, 2011). We also note that, unlike the rest, the estimate of Stephenson et al. (1995) is based on the analysis of the Earth's rotational data over the recent centuries, which features a much larger uncertainty compared to other studies. Right: Level curves of the surface of computed \dot{J}_2 on a grid of combinations of viscosity values for the upper and lower mantle parts. We specified curves corresponding to relevant limits of observational values.

suggesting nonlinearity (Cheng et al., 2013). The likely cause of this swing was attributed to modern melting of glaciers as an outcome of global warming (Chao et al., 2020; Loomis et al., 2019; Matsuo et al., 2013; Roy & Peltier, 2011). It is suggested that obtaining a pure GIA signal of \dot{J}_2 requires isolating this “contamination” of glaciers' modern melting (Ivins et al., 1993). This can lead to a pure GIA contribution of larger negative values (e.g., $-5.4 \pm 0.7 \times 10^{-11} \text{ yr}^{-1}$ [Lau et al., 2016]; $-(6.0-6.5) \times 10^{-11} \text{ yr}^{-1}$ [Nakada et al., 2015]). However, in our effective model, we restrict our study to the trend of \dot{J}_2 before the departure from linearity, and we consider this trend to be a pure GIA signal (Roy & Peltier, 2011).

On a grid covering the ranges of mantle viscosity values (Figure 5), and using the already developed ice distribution, we compute present day rates of variation of J_2 . In Figure 7, we contour the surface of \dot{J}_2 in this effective viscosity space, and we specify level curves of relevance with respect to the observed values. The latter appear to be concentrated around two regions, which as discussed earlier, are mostly dependent on the lower mantle viscosity. This sensitivity is clear with the vertical structure of the level curves. Thus in total, two regions of viscosity combinations are preferred for the best fit with observational data: \mathcal{R}_1 , a region enclosed by $\log_{10} \nu_{LM} \in [21.2, 21.6]$ for any value of ν_{UM} , and a region \mathcal{R}_2 , enclosed by $\log_{10} \nu_{LM} \in [23.1, 23.6]$ with large values of upper mantle viscosity. \mathcal{R}_2 diverges for lower values of upper mantle viscosity corresponding to an Earth with a very acute jump between the mantle parts (three to four orders of magnitude). Thus for values of upper mantle viscosity well constrained within the shaded region of Figure 5, \mathcal{R}_1 best fits the observed \dot{J}_2 . Moreover, as explained earlier, the region \mathcal{R}_2 is ruled out by taking the second rotational datum into account (Argus et al., 2021; Peltier, 2015). Namely, modern observations of the speed ($0.98^\circ \text{ Myr}^{-1}$) and direction (79.9° W) of the true polar wander (Argus & Gross, 2004) can only be fitted using low viscosity-contrast models. We identified \mathcal{R}_1 in the dynamical ellipticity evolution space in Figure 6. This region is consistent with the inferred low contrast viscosity profiles: VM5a (Peltier et al., 2015), VM7 (Roy & Peltier, 2017), and that of Lau et al. (2016). This trapezoidal region represents our constrained estimates for the average and amplitude of the variation in the dynamical ellipticity. It clearly shows that the pure GIA contribution cannot drive the Earth into the $s_6 - g_6 + g_5$ resonance.

6. Summary and Conclusion

In this article, we provide the evolution of the dynamical ellipticity of the Earth over the past 47 Myr due to the varying glacial surface load. We revisit this problem identifying the major sensitivities of the dynamical ellipticity to surface loading and internal viscoelastic response. Concerning glacial history, we use a recently compiled far-field record of benthic oxygen isotopes that covers the Cenozoic (Miller et al., 2020). As both ocean temperature and ice volume take part in the isotopic variation, the contributions are deconvolved using benthic Mg/Ca records as an independent temperature proxy. We here consider that the glacial contribution of the isotopic record is an estimate of global ice volume, but we proceed with caution noting the following:

1. This is only a rough estimate that gains more precision when accompanied by a record of oxygen isotope composition in the ice sheets (Langebroek et al., 2010).
2. Our inference of the global glacial volume from the isotopic record could be compromised by variations in atmospheric moisture transport and the thickness of ice sheets yielding an overestimate of glacial volume (Winnick & Caves, 2015). Uncertainties in using this isotope record can also propagate from the used temperature contribution correction (Cramer et al., 2011), especially given evidence on discrepancies between ice growth reconstruction and the isotopic record over the last glacial cycle (Pico et al., 2017), or over the Pliocene (Gasson, DeConto, & Pollard, 2016).
3. The comparison of the sea level equivalent of the record with the sea level construction from continental margins (Miller et al., 2020) can also be compromised by effects of mantle dynamic topography rather than pure glacial dynamics (Forte et al., 1993; Moucha et al., 2008).
4. However, our ice sensitivity tests proved that the correction to the dynamical ellipticity evolution due to an ice uncertainty propagating from an error of ± 20 m in eustatic sea level equivalence does not corrupt model predictions (Figure 3). Moreover, uncertainties in the spatial distribution of ice are minimized by the symmetries of the second zonal harmonic. The geological evidence employed (see Table 1) is also a critical backbone of the analysis we report here.

Based on this ice history, we used the SLE solver of Spada and Melini (2019) to self-consistently trace the evolution of the surface loading between the ice caps and the oceans. On the other hand, the viscoelastic response of the Earth features the major variable in the problem. The evolution of the dynamical ellipticity mostly depends on the Earth's viscosity profile, specifically on the lower mantle viscosity. We considered a single effective viscosity for the lower mantle and studied its dependence in Figure 6, and then proceeded with a misfit analysis of model predictions of J_2 with recent observational estimates (Figure 7). The final outcome is constraining the average relative perturbation in the dynamical ellipticity over the past 3 Myr to $[-0.031\%, -0.055\%]$, with a lower boundary inside $[-0.07\%, -0.13\%]$, and a less sensitive upper limit around $+0.07\%$ (Figure 6). These intervals account for an uncertainty propagating from the used ice distribution. Scrutinizing our model dynamical ellipticity perturbation evolution over the past 700 kyr, and using the same viscosity profiles, our mean and peak-to-peak estimates are smaller than those computed by Mitrova and Forte (1995) (for the averaged viscosity profile of Mitrova & Forte, 2004, our maximum negative perturbation of $\delta H/H_0$ is -0.21% , while their maximum is -0.3%). In contrast, our estimates are larger than those less acute in Peltier and Jiang (1994). Our evolution extends to the mostly unipolar interval of the Cenozoic with an average inside $[-0.02\%, -0.045\%]$. Going beyond 47 Ma, our ice input, and consequently our ellipticity evolution are compromised by the growing error in the Mg/Ca record.

This constrained history of the dynamical ellipticity will be used in the future long term numerical solutions for the orbital and rotational quantities of the Earth, entering through a time-dependent variation of the precession “constant” (Equation 4; Laskar, Fienga, et al., 2011; Laskar et al., 2004). Our model predictions of the surface loading effect alone preclude the possibility of a past crossing of resonance with Jupiter and Saturn through the $s_6 - g_6 + g_5$ mode described in Section 2. Besides the surface loading, redistribution of mass within the Earth due to mantle convection also contributes to the evolution of the dynamical ellipticity. Such a contribution is also dependent on the viscosity profile. However, at present, different methods of recovering the past mantle flow yielded vastly different results, albeit using the same viscosity profile (Forte & Mitrova, 1997; Ghelichkhan et al., 2020; Morrow et al., 2012). Moreover, the backward tidal evolution of the Earth's rotational velocity counteracts the effect of dynamical ellipticity variation, driving the precession frequency away from this resonance. Thus a thorough and realistic study of such a resonance encounter in the past requires a self-consistent model that combines all three elements, leaving us with the need for more effort in this direction.

Appendix A: The Centrifugal Potential Variation

In addition to the direct effect of surface loading, the dynamical ellipticity is also subject to variation due to the varying centrifugal potential, as a consequence of altering the magnitude and direction of the angular velocity vector due to the mass redistribution. This rotational effect was one of the additions that came about during the development of the sea level variation theory. However, on the basis of the following approximations, we argue that this effect is minimal on the dynamical ellipticity, and we decided to ignore it in our calculations. It should be stressed that the variation of the angular velocity discussed here is merely related to the mass redistribution associated with surface loading. On the other hand, the angular velocity variation associated with the tidal interaction between the Earth and the Moon is the dominant contributor to the precession “constant” evolution over geological timescales; an effect that falls outside the scope of this discussion.

Considering the rotating Earth and aligning the angular velocity vector $\vec{\omega}$ along the z -axis, one can write the centrifugal potential felt by a point P at the surface that is, in the co-rotating frame as:

$$V^c(P) = \frac{1}{2}\omega^2 r_p^2 = \frac{1}{2}\omega^2 a^2 (1 - \cos^2\theta_p) \quad (A1)$$

where θ_p is the angular separation of P from the axis of rotation. Using the Legendre polynomials, this can be written as:

$$V^c(P) = \frac{\omega^2 a^2}{3} (P_0(\cos\theta_p) - P_2(\cos\theta_p)). \quad (A2)$$

The theory usually continues by expanding the potential variation into variations in the angular velocity vector, and to leading terms in the perturbation, this expansion is used in the problem of the true polar wander and solving Liouville equations (Sabadini et al., 2016). But for our purposes here, we are considering only the variations in the second zonal harmonic. In a general sense, the variation in the dynamical ellipticity H due to variations in the surface loading potential V^L , and centrifugal potential V^c can be derived from:

$$\begin{aligned} H &= \frac{a^3}{GC} (1 + k_2^L) V_2^L + \frac{a^3}{GC} k_2^T V_2^c \\ &= \frac{a^3}{GC} (1 + k_2^L) V_2^L + k_2^T \frac{\omega^2 a^5}{3GC} \end{aligned} \quad (A3)$$

where a is the Earth's radius, G is the gravitational constant, C is the polar moment of inertia, k_2^L and k_2^T are the loading and tidal Love numbers, and $\omega = |\vec{\omega}|$. The variation in the potential is driven by variations in the polar moment of inertia on the following basis: A rigid Earth variation written as:

$$\delta C^r = \frac{2a^3}{3G} \delta V_2^L \quad (A4)$$

the viscoelastic compensation depicted in:

$$\delta C^{ve} = \frac{2a^3}{3G} k_2^L \delta V_2^L = k_2^L \delta C^r \quad (A5)$$

and the rotation effect:

$$\delta C^{rot} = \frac{2a^3}{3G} k_2^T \delta V_2^c = \frac{4a^5}{9G} k_2^T \omega \delta \omega. \quad (A6)$$

In a general sense too, the dynamical ellipticity can be split into the hydrostatic component H^f , and a residual part δH depending on all possible surface and internal irregularities:

$$H = H^f + \delta H \quad (A7)$$

where the hydrostatic part can be found by taking the fluid limit of Equation A3:

$$\begin{aligned} H^f &= \frac{a^3}{GC} (1 + k_2^{L,f}) V_2^L + k_2^{T,f} \frac{a^5}{3GC} \omega^2 \\ &\approx k_2^{T,f} \frac{a^5}{3GC} \omega^2 \end{aligned} \quad (A8)$$

where the last approximation is possible since $k_2^{L,f} \approx -0.98$ while $k_2^{T,f} \approx 0.97$. Ignoring the loss of angular momentum due to tidal dissipation, the variation in the angular velocity or the length of the day is accompanied by a variation in the moment of inertia to conserve the angular momentum, thus we can write:

$$\begin{aligned} \delta(C\omega) &= C\delta\omega + \omega(1+k_2^L)\delta C^r + \omega\delta C^{\text{rot}} \\ &= \delta\omega\left(C + \frac{4a^5}{9G}k_2^T\omega^2\right) + (1+k_2^L)\omega\delta C^r \\ &= \delta\omega C\left(1 + \frac{4}{3}\frac{k_2^T}{k_2^{T,f}}H^f\right) + (1+k_2^L)\omega\delta C^r \\ &\approx \delta\omega C + (1+k_2^L)\omega\delta C^r \equiv 0 \end{aligned} \quad (\text{A9})$$

where the approximation was based on the relatively small value of H^f . This allows us to write:

$$\delta\omega \approx -(1+k_2^L)\omega\frac{\delta C^r}{C}. \quad (\text{A10})$$

With these quantities, we can finally compute the ratio of the contributions to the polar inertia variation as:

$$\left|\frac{\delta C^{\text{rot}}}{(1+k_2^L)\delta C^r}\right| = \left|\frac{4a^5\omega^2}{9GC}k_2^T\right| = \left|\frac{4k_2^T}{3k_2^{T,f}}H^f\right| \approx 10^{-3} \quad (\text{A11})$$

where $k_2^T \approx 0.3$, $k_2^{T,f} \approx 0.97$, and $H^f \approx 3 \times 10^{-3}$. On this basis, we ignored the effect of rotation on the perturbation of dynamical ellipticity in our simulations.

Appendix B: The Cenozoic Spatial Distribution of Ice

As discussed in the main text, the glacial surface loading function is discretized spatially in order to facilitate the computation of the surface integrals by the pseudo spectral approach (Mitrovica & Peltier, 1991). The global estimate of ice volume, M20 (Miller et al., 2020), is thus distributed over the spherically pixelated grid on the surface of the Earth. SELEN⁴ adopts the grid of the equal-area, icosahedron-shaped pixels (Tegmark, 1996). This grid is characterized by a resolution parameter R such that the total number of pixels on the surface P is:

$$P = 40R(R-1) + 12. \quad (\text{B1})$$

All our simulations were performed with $R = 30$, yielding $P = 34,812$. For such a large number of pixels, each pixel can be thought of as a disk of radius $r_{\text{disk}} \approx 2a/\sqrt{P}$. Thus each pixel approximately covers a surface area of 14,600 km².

In the main text, we identified major milestones of ice variability based on a compilation of available geologic evidence and GCMs (Table 1). Over the time interval of our simulations (47 Myr), we scale our glacial input with the global limit of M20, however, we separate between eight intervals of spatial spread. Samples of the spread over these intervals are plotted via MATLAB's Mapping Toolbox (Greene et al., 2017) and shown in Figure B1 for the AIS, and in Figure B2 of the northern ice sheets. Before the EOT, ice is distributed over the high elevation regions of the East Antarctic Ice Sheet (EAIS); specifically on the Dronning Maud Land, the Gamburtsev Mountains, and parts of the Trans-Antarctic Mountains (Gulick et al., 2017; Rose et al., 2013), along with partial glaciation on the south-east end of Greenland (Eldrett et al., 2007; Tripathi & Darby, 2018). The second interval, the Oligocene, witnesses continental scale spread on the EAIS (DeConto & Pollard, 2003), with minimal glaciation on the high elevation plateaus of the western part (WAIS; Rocchi et al., 2006; Sorlien et al., 2007), and on the Eastern side of the Greenland Ice Sheet (GIS). The third interval, covering the Early Miocene, only differs from the second interval by the expansion of the EAIS into marine terminating glacial spread (Bart, 2003; Bartek et al., 1992). The fourth interval represents the warm period of the MMCO, and is characterized by Antarctic glacial retreat reaching the spread of the first interval (Levy et al., 2016). Following the MMCO, the stable EAIS is established, and ice fully covers the WAIS and the GIS for the first time (Shakun et al., 2018). The sixth interval represents the warm period of the Early Pliocene, and it witnessed the retreat of the WAIS and Greenland (Cook et al., 2013; Naish et al., 2009). Starting 3 Ma, the seventh interval highlights the maximum glacial spread over

the Cenozoic, with the glaciation of the Laurentide and the Fennoscandia ice sheets (Figure B2). In this interval, for the separation of the global ice volume between the northern and southern regions, we use the simulation of Pollard and DeConto (2009) as an estimate of Antarctic ice. Subtracting this estimate from the global limit leaves us with the contribution of the northern cap. Finally, we terminate our established history with the ICE-6G model (Peltier et al., 2015), and we use the spread of the LGM as the limit of the maximum possible ice spread. In each interval, the distribution of the allocated ice volume over the pixels of the corresponding region is controlled by the relative distribution among the same pixels at the LGM.

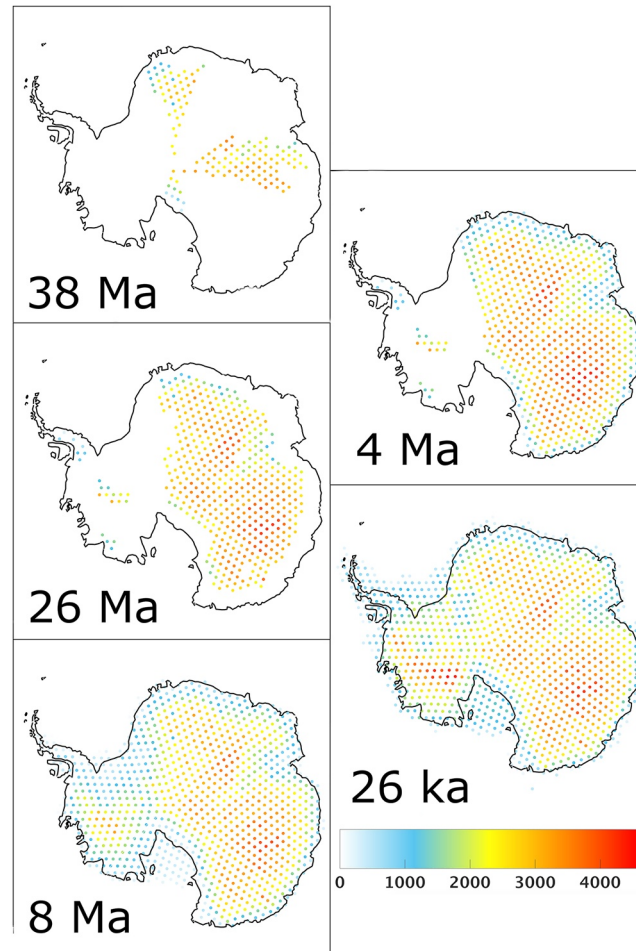


Figure B1. Time slices of the Antarctic ice distribution on the pixelated surface of the Earth. Color coding represents the ice thickness in meters. Each spatial spread is used over a specific interval of time (see text).

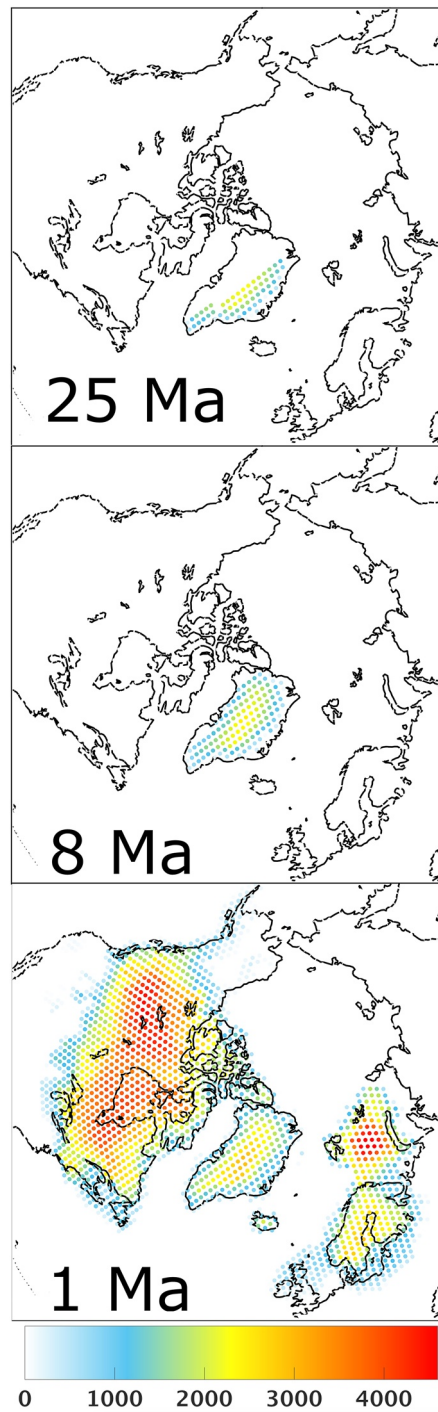


Figure B2. Same as Figure B1, but for the glacial spread over the Northern Hemisphere.

Data Availability Statement

The Cenozoic $\delta^{18}\text{O}_{\text{benthic}}$ record used in this work is available through Miller et al. (2020) and the Supporting Information files therein. Schemes of the Earth's surface pixelization are included in the repository of SELEN⁴ (Spada & Melini, 2019).

Acknowledgments

This work was granted access to the HPC resources of MesoPSL financed by the Region Ile de France and the project Equip²Meso (reference ANR-10-EQPX-29-01) of the programme Investissements d'Avenir supervised by the Agence Nationale pour la Recherche. It has also received funding from the European Research Council (ERC) under the European Union's Horizon 2020 research and innovation programme (Advanced Grant AstroGeo-885250) and from the Agence Nationale pour la Recherche (ANR; Grant AstroMeso ANR-19-CE31-0002-01).

References

- Adhikari, S., Caron, L., Steinberger, B., Reager, J. T., Kjeldsen, K. K., Marzeion, B., et al. (2018). What drives 20th century polar motion? *Earth and Planetary Science Letters*, 502, 126–132. <https://doi.org/10.1016/j.epsl.2018.08.059>
- Adhikari, S., Ivins, E. R., & Larour, E. (2016). ISSM-SESAW v1. 0: Mesh-based computation of gravitationally consistent sea level and geodetic signatures caused by cryosphere and climate driven mass change. *Geoscientific Model Development*, 9(3), 1087–1109. <https://doi.org/10.5194/gmd-9-1087-2016>
- Argus, D. F., & Gross, R. S. (2004). An estimate of motion between the spin axis and the hotspots over the past century. *Geophysical Research Letters*, 31(6), L06614. <https://doi.org/10.1029/2004gl019657>
- Argus, D. F., Peltier, W. R., Blewitt, G., & Kreemer, C. (2021). The viscosity of the top third of the lower mantle estimated using GPS, grace, and relative sea level measurements of glacial isostatic adjustment. *Journal of Geophysical Research: Solid Earth*, 126(5), e2020JB021537. <https://doi.org/10.1029/2020jb021537>
- Austermann, J., Mitrovica, J. X., Latychev, K., & Milne, G. A. (2013). Barbados-based estimate of ice volume at last glacial maximum affected by subducted plate. *Nature Geoscience*, 6(7), 553–557. <https://doi.org/10.1038/ngeo1859>
- Bart, P. J. (2003). Were West Antarctic Ice Sheet grounding events in the Ross Sea a consequence of East Antarctic Ice Sheet expansion during the middle Miocene? *Earth and Planetary Science Letters*, 216(1–2), 93–107. [https://doi.org/10.1016/s0012-821x\(03\)00509-0](https://doi.org/10.1016/s0012-821x(03)00509-0)
- Bartek, L., Sloan, L. C., Anderson, J., & Ross, M. (1992). Evidence from the Antarctic continental margin of late Paleogene ice sheets: A manifestation of plate reorganization and synchronous changes in atmospheric circulation over the emerging Southern Ocean. *Eocene-Oligocene climatic and biotic evolution* (pp. 131–159). Princeton University Press.
- Berger, A. (1988). Milankovitch theory and climate. *Reviews of geophysics*, 26(4), 624–657. <https://doi.org/10.1029/rg026i004p00624>
- Bouhila, S., Galbrun, B., Miller, K. G., Pekar, S. F., Browning, J. V., Laskar, J., & Wright, J. D. (2011). On the origin of Cenozoic and Mesozoic “third-order” eustatic sequences. *Earth-Science Reviews*, 109(3–4), 94–112. <https://doi.org/10.1016/j.earscirev.2011.09.003>
- Burša, M., Groten, E., & Šima, Z. (2008). Steady change in flattening of the Earth: The precession constant and its long term variation. *The Astronomical Journal*, 135(3), 1021–1023. <https://doi.org/10.1088/0004-6256/135/3/1021>
- Chambat, F., Ricard, Y., & Valette, B. (2010). Flattening of the Earth: Further from hydrostaticity than previously estimated. *Geophysical Journal International*, 183(2), 727–732. <https://doi.org/10.1111/j.1365-246x.2010.04771.x>
- Chao, B., Yu, Y., & Chung, C. (2020). Variation of Earth's oblateness J_2 on interannual-to-decadal timescales. *Journal of Geophysical Research: Solid Earth*, 125(6), e2020JB019421. <https://doi.org/10.1029/2020jb019421>
- Cheng, M., Eanes, R., Shum, C., Schutz, B., & Tapley, B. (1989). Temporal variations in low degree zonal harmonics from Starlette orbit analysis. *Geophysical Research Letters*, 16(5), 393–396. <https://doi.org/10.1029/g1016i005p00393>
- Cheng, M., Tapley, B. D., & Ries, J. C. (2013). Deceleration in the Earth's oblateness. *Journal of Geophysical Research: Solid Earth*, 118(2), 740–747. <https://doi.org/10.1002/jgrb.50058>
- Clark, J. A., Farrell, W. E., & Peltier, W. R. (1978). Global changes in postglacial sea level: A numerical calculation. *Quaternary Research*, 9(3), 265–287. [https://doi.org/10.1016/0033-5894\(78\)90033-9](https://doi.org/10.1016/0033-5894(78)90033-9)
- Cleveland, W. S., & Devlin, S. J. (1988). Locally weighted regression: An approach to regression analysis by local fitting. *Journal of the American Statistical Association*, 83(403), 596–610. <https://doi.org/10.1080/01621459.1988.10478639>
- Conrad, C. P. (2013). The solid Earth's influence on sea level. *Bulletin*, 125(7–8), 1027–1052. <https://doi.org/10.1130/b30764.1>
- Cook, C. P., Van De Fliedert, T., Williams, T., Hemming, S. R., Iwai, M., Kobayashi, M., et al. (2013). Dynamic behavior of the East Antarctic Ice Sheet during Pliocene warmth. *Nature Geoscience*, 6(9), 765–769. <https://doi.org/10.1038/ngeo1889>
- Cox, C. M., & Chao, B. F. (2002). Detection of a large scale mass redistribution in the terrestrial system since 1998. *Science*, 297(5582), 831–833. <https://doi.org/10.1126/science.1072188>
- Coxall, H. K., Wilson, P. A., Pälike, H., Lear, C. H., & Backman, J. (2005). Rapid stepwise onset of Antarctic glaciation and deeper calcite compensation in the Pacific Ocean. *Nature*, 433(7021), 53–57. <https://doi.org/10.1038/nature03135>
- Cramer, B., Miller, K., Barrett, P., & Wright, J. (2011). Late Cretaceous-Neogene trends in deep ocean temperature and continental ice volume: Reconciling records of benthic foraminiferal geochemistry ($\delta^{18}\text{O}$ and Mg/Ca) with sea level history. *Journal of Geophysical Research: Oceans*, 116(C12), C12023. <https://doi.org/10.1029/2011jc007255>
- Daly, R. A. (1925). Pleistocene changes of level. *American Journal of Science*, 10(58), 281–313. <https://doi.org/10.2475/ajs.s5-10.58.281>
- DeConto, R. M., & Pollard, D. (2003). Rapid Cenozoic glaciation of Antarctica induced by declining atmospheric CO_2 . *Nature*, 421(6920), 245–249. <https://doi.org/10.1038/nature01290>
- DeConto, R. M., Pollard, D., Wilson, P. A., Pälike, H., Lear, C. H., & Pagani, M. (2008). Thresholds for Cenozoic bipolar glaciation. *Nature*, 455(7213), 652–656. <https://doi.org/10.1038/nature07337>
- Dehant, V., Loutre, M.-F., & Berger, A. (1990). Potential impact of the Northern Hemisphere quaternary ice sheets on the frequencies of the astronomical orbital parameters. *Journal of Geophysical Research: Atmospheres*, 95(D6), 7573–7578. <https://doi.org/10.1029/jd095id06p07573>
- De Vleeschouwer, D., Vahlenkamp, M., Crucifix, M., & Pälike, H. (2017). Alternating Southern and Northern Hemisphere climate response to astronomical forcing during the past 35 m.y. *Geology*, 45(4), 375–378. <https://doi.org/10.1130/g38663.1>
- Dziewonski, A. M., & Anderson, D. L. (1981). Preliminary reference Earth model. *Physics of the Earth and Planetary Interiors*, 25(4), 297–356. [https://doi.org/10.1016/0031-9201\(81\)90046-7](https://doi.org/10.1016/0031-9201(81)90046-7)
- Eldrett, J. S., Harding, I. C., Wilson, P. A., Butler, E., & Roberts, A. P. (2007). Continental ice in Greenland during the Eocene and Oligocene. *Nature*, 446(7132), 176–179. <https://doi.org/10.1038/nature05591>
- Farrell, W. E., & Clark, J. A. (1976). On postglacial sea level. *Geophysical Journal International*, 46(3), 647–667. <https://doi.org/10.1111/j.1365-246x.1976.tb01252.x>
- Forté, A. M., & Mitrovica, J. (1997). A resonance in the Earth's obliquity and precession over the past 20 Myr driven by mantle convection. *Nature*, 390(6661), 676–680. <https://doi.org/10.1038/37769>
- Forté, A. M., Moucha, R., Rowley, D., Quééré, S., Mitrovica, J., Simmons, N., & Grand, S. (2009). Recent tectonic plate decelerations driven by mantle convection. *Geophysical Research Letters*, 36(23), L23301. <https://doi.org/10.1029/2009gl040224>
- Forté, A. M., Peltier, W., Dziewonski, A., & Woodward, R. (1993). Dynamic surface topography: A new interpretation based upon mantle flow models derived from seismic tomography. *Geophysical Research Letters*, 20(3), 225–228. <https://doi.org/10.1029/93gl00249>
- Galeotti, S., DeConto, R., Naish, T., Stocchi, P., Florindo, F., Pagani, M., et al. (2016). Antarctic ice sheet variability across the Eocene-Oligocene boundary climate transition. *Science*, 352(6281), 76–80. <https://doi.org/10.1126/science.aab0669>
- Gasparini, P., Dal Forno, G., & Boschi, E. (2004). Linear or nonlinear rheology in the Earth's mantle: The prevalence of power law creep in the postglacial isostatic readjustment of Laurentia. *Geophysical Journal International*, 157(3), 1297–1302. <https://doi.org/10.1111/j.1365-246x.2004.02319.x>

- Gasson, E., DeConto, R. M., & Pollard, D. (2016). Modeling the oxygen isotope composition of the Antarctic ice sheet and its significance to Pliocene sea level. *Geology*, 44(10), 827–830. <https://doi.org/10.1130/g38104.1>
- Gasson, E., DeConto, R. M., Pollard, D., & Levy, R. H. (2016). Dynamic Antarctic ice sheet during the early to mid-Miocene. *Proceedings of the National Academy of Sciences*, 113(13), 3459–3464. <https://doi.org/10.1073/pnas.1516130113>
- Ghelichkhan, S., Fuentes, J. J., Hoggard, M. J., Richards, F. D., & Mitrovica, J. (2020). The precession constant and its long term variation. *Icarus*, 358, 114172. <https://doi.org/10.1016/j.icarus.2020.114172>
- Gradstein, F. M., Ogg, J. G., Schmitz, M., & Ogg, G. (2012). *The geologic time scale 2012* (Vol. 2). Elsevier.
- Gradstein, F. M., Ogg, J. G., Schmitz, M., & Ogg, G. (2020). *Geologic time scale 2020* (Vol. 2). Elsevier.
- Gradstein, F. M., Ogg, J. G., & Smith, A. G. (2004). *A geologic time scale 2004*. Cambridge University Press.
- Greene, C. A., Gwyther, D. E., & Blankenship, D. D. (2017). Antarctic mapping tools for MATLAB. *Computers & Geosciences*, 104, 151–157. <https://doi.org/10.1016/j.cageo.2016.08.003>
- Gulick, S. P., Shevenell, A. E., Montelli, A., Fernandez, R., Smith, C., Warny, S., et al. (2017). Initiation and long term instability of the East Antarctic Ice Sheet. *Nature*, 552(7684), 225–229. <https://doi.org/10.1038/nature25026>
- Hauptvogel, D., Pekar, S., & Pincay, V. (2017). Evidence for a heavily glaciated Antarctica during the late Oligocene “warming” (27.8–24.5 Ma): Stable isotope records from ODP site 690. *Paleoceanography*, 32(4), 384–396. <https://doi.org/10.1002/2016pa002972>
- Heiskanen, W. A. (1967). Physical geodesy. *Determination of the Geoid From Ground Anomalies*, 8, 325–330.
- Huber, B. T., MacLeod, K. G., Watkins, D. K., & Coffin, M. F. (2018). The rise and fall of the Cretaceous Hot Greenhouse climate. *Global and Planetary Change*, 167, 1–23. <https://doi.org/10.1016/j.gloplacha.2018.04.004>
- Ivins, E. R., Sammis, C., & Yoder, C. (1993). Deep mantle viscous structure with prior estimate and satellite constraint. *Journal of Geophysical Research: Solid Earth*, 98(B3), 4579–4609. <https://doi.org/10.1029/92jb02728>
- Kendall, R. A., Mitrovica, J. X., & Milne, G. A. (2005). On postglacial sea level—II. Numerical formulation and comparative results on spherically symmetric models. *Geophysical Journal International*, 161(3), 679–706. <https://doi.org/10.1111/j.1365-246x.2005.02553.x>
- Kominz, M. A., Browning, J., Miller, K., Sugarman, P., Mizintseva, S., & Scotese, C. (2008). Late Cretaceous to Miocene sea level estimates from the New Jersey and Delaware coastal plain coreholes: An error analysis. *Basin Research*, 20(2), 211–226. <https://doi.org/10.1111/j.1365-2117.2008.00354.x>
- Lambeck, K., Purcell, A., & Zhao, S. (2017). The North American late Wisconsin ice sheet and mantle viscosity from glacial rebound analyses. *Quaternary Science Reviews*, 158, 172–210. <https://doi.org/10.1016/j.quascirev.2016.11.033>
- Lambeck, K., Rouby, H., Purcell, A., Sun, Y., & Sambridge, M. (2014). Sea level and global ice volumes from the last glacial maximum to the Holocene. *Proceedings of the National Academy of Sciences*, 111(43), 15296–15303. <https://doi.org/10.1073/pnas.1411762111>
- Langebroek, P. M., Paul, A., & Schulz, M. (2009). Antarctic ice-sheet response to atmospheric CO₂ and insolation in the middle Miocene. *Climate of the Past*, 5(4), 633–646. <https://doi.org/10.5194/cp-5-633-2009>
- Langebroek, P. M., Paul, A., & Schulz, M. (2010). Simulating the sea level imprint on marine oxygen isotope records during the middle Miocene using an ice sheet-climate model. *Paleoceanography*, 25(4). <https://doi.org/10.1029/2008pa001704>
- Laskar, J. (1989). A numerical experiment on the chaotic behavior of the solar system. *Nature*, 338(6212), 237–238. <https://doi.org/10.1038/338237a0>
- Laskar, J., Fienga, A., Gastineau, M., & Manche, H. (2011). La2010: A new orbital solution for the long term motion of the Earth. *Astronomy & Astrophysics*, 532, A89. <https://doi.org/10.1051/0004-6361/201116836>
- Laskar, J., Gastineau, M., Delisle, J.-B., Farrés, A., & Fienga, A. (2011). Strong chaos induced by close encounters with Ceres and Vesta. *Astronomy & Astrophysics*, 532, L4. <https://doi.org/10.1051/0004-6361/201117504>
- Laskar, J., Joutel, F., & Boudin, F. (1993). Orbital, precessional, and insolation quantities for the Earth from –20 to +10 Myr. *Astronomy and Astrophysics*, 270, 522–533.
- Laskar, J., & Robutel, P. (1993). The chaotic obliquity of the planets. *Nature*, 361(6413), 608–612. <https://doi.org/10.1038/361608a0>
- Laskar, J., Robutel, P., Joutel, F., Gastineau, M., Correia, A., & Levrard, B. (2004). A long term numerical solution for the insolation quantities of the Earth. *Astronomy & Astrophysics*, 428(1), 261–285. <https://doi.org/10.1051/0004-6361/20041335>
- Lau, H. C., Mitrovica, J., Austermann, J., Crawford, O., Al-Attar, D., & Latychev, K. (2016). Inferences of mantle viscosity based on ice age data sets: Radial structure. *Journal of Geophysical Research: Solid Earth*, 121(10), 6991–7012. <https://doi.org/10.1002/2016jb013043>
- Lear, C. H., Elderfield, H., & Wilson, P. (2000). Cenozoic deep-sea temperatures and global ice volumes from Mg/Ca in benthic foraminiferal calcite. *Science*, 287(5451), 269–272. <https://doi.org/10.1126/science.287.5451.269>
- Levrard, B., & Laskar, J. (2003). Climate friction and the Earth’s obliquity. *Geophysical Journal International*, 154(3), 970–990. <https://doi.org/10.1046/j.1365-246x.2003.02021.x>
- Levy, R., Harwood, D., Florindo, F., Sangiorgi, F., Tripati, R., Von Eynatten, H., et al. (2016). Antarctic ice sheet sensitivity to atmospheric CO₂ variations in the early to mid-Miocene. *Proceedings of the National Academy of Sciences*, 113(13), 3453–3458. <https://doi.org/10.1073/pnas.1516030113>
- Liebrand, D., deBakker, A. T., Beddow, H. M., Wilson, P. A., Bohaty, S. M., Ruessink, G., et al. (2017). Evolution of the early Antarctic ice ages. *Proceedings of the National Academy of Sciences*, 114(15), 3867–3872. <https://doi.org/10.1073/pnas.1615440114>
- Loomis, B., Rachlin, K., & Luthcke, S. (2019). Improved Earth oblateness rate reveals increased ice sheet losses and mass-driven sea level rise. *Geophysical Research Letters*, 46(12), 6910–6917. <https://doi.org/10.1029/2019gl082929>
- Lourens, L. J., Wehausen, R., & Brumsack, H. J. (2001). Geological constraints on tidal dissipation and dynamical ellipticity of the Earth over the past 3 Myr. *Nature*, 409(6823), 1029–1033. <https://doi.org/10.1038/35059062>
- Lynch-Stieglitz, J., Curry, W. B., & Slowey, N. (1999). A geostrophic transport estimate for the Florida current from the oxygen isotope composition of benthic foraminifera. *Paleoceanography*, 14(3), 360–373. <https://doi.org/10.1029/1999pa000001>
- Mathews, P. M., Herring, T. A., & Buffett, B. A. (2002). Modeling of nutation and precession: New nutation series for nonrigid Earth and insights into the Earth’s interior. *Journal of Geophysical Research: Solid Earth*, 107(B4). ETG 3-1–ETG 3-26. <https://doi.org/10.1029/2001jb000390>
- Matsuo, K., Chao, B. F., Otsubo, T., & Heki, K. (2013). Accelerated ice mass depletion revealed by low-degree gravity field from satellite laser ranging: Greenland, 1991–2011. *Geophysical Research Letters*, 40(17), 4662–4667. <https://doi.org/10.1002/grl.50900>
- Miller, K. G., Browning, J. V., Schmelz, W. J., Kopp, R. E., Mountain, G. S., & Wright, J. D. (2020). Cenozoic sea level and cryospheric evolution from deep-sea geochemical and continental margin records. *Science Advances*, 6(20), eaaz1346. <https://doi.org/10.1126/sciadv.aaz1346>
- Miller, K. G., Fairbanks, R. G., & Mountain, G. S. (1987). Tertiary oxygen isotope synthesis, sea level history, and continental margin erosion. *Paleoceanography*, 2(1), 1–19. <https://doi.org/10.1029/pa002i001p00001>
- Miller, K. G., Wright, J. D., Browning, J. V., Kulpecz, A., Kominz, M., Naish, T. R., et al. (2012). High tide of the warm Pliocene: Implications of global sea level for Antarctic deglaciation. *Geology*, 40(5), 407–410. <https://doi.org/10.1130/g32869.1>

- Milne, G. A., & Mitrovica, J. X. (1998). Postglacial sea level change on a rotating Earth. *Geophysical Journal International*, 133(1), 1–19. <https://doi.org/10.1046/j.1365-246x.1998.1331455.x>
- Mitrovica, J. X., & Forte, A. M. (1995). Pleistocene glaciation and the Earth's precession constant. *Geophysical Journal International*, 121(1), 21–32. <https://doi.org/10.1111/j.1365-246x.1995.tb03508.x>
- Mitrovica, J. X., & Forte, A. M. (1997). Radial profile of mantle viscosity: Results from the joint inversion of convection and postglacial rebound observables. *Journal of Geophysical Research: Solid Earth*, 102(B2), 2751–2769. <https://doi.org/10.1029/96jb03175>
- Mitrovica, J. X., & Forte, A. M. (2004). A new inference of mantle viscosity based upon joint inversion of convection and glacial isostatic adjustment data. *Earth and Planetary Science Letters*, 225(1–2), 177–189. <https://doi.org/10.1016/j.epsl.2004.06.005>
- Mitrovica, J. X., Forte, A. M., & Pan, R. (1997). Glaciation-induced variations in the Earth's precession frequency, obliquity and insolation over the last 2.6 Ma. *Geophysical Journal International*, 128(2), 270–284. <https://doi.org/10.1111/j.1365-246x.1997.tb01554.x>
- Mitrovica, J. X., & Milne, G. (2003). On postglacial sea level: I. General theory. *Geophysical Journal International*, 154(2), 253–267. <https://doi.org/10.1046/j.1365-246x.2003.01942.x>
- Mitrovica, J. X., & Peltier, W. (1989). Pleistocene deglaciation and the global gravity field. *Journal of Geophysical Research: Solid Earth*, 94(B10), 13651–13671. <https://doi.org/10.1029/jb094ib10p13651>
- Mitrovica, J. X., & Peltier, W. R. (1991). On postglacial geoid subsidence over the equatorial oceans. *Journal of Geophysical Research: Solid Earth*, 96(B12), 20053–20071. <https://doi.org/10.1029/91jb01284>
- Mitrovica, J. X., & Peltier, W. R. (1993). The inference of mantle viscosity from an inversion of the Fennoscandian relaxation spectrum. *Geophysical Journal International*, 114(1), 45–62. <https://doi.org/10.1111/j.1365-246x.1993.tb01465.x>
- Morrow, E., Mitrovica, J., Forte, A., Glišović, P., & Huybers, P. (2012). An enigma in estimates of the Earth's dynamic ellipticity. *Geophysical Journal International*, 191(3), 1129–1134.
- Moucha, R., Forte, A. M., Mitrovica, J., Rowley, D. B., Quéré, S., Simmons, N. A., & Grand, S. P. (2008). Dynamic topography and long term sea level variations: There is no such thing as a stable continental platform. *Earth and Planetary Science Letters*, 271(1–4), 101–108. <https://doi.org/10.1016/j.epsl.2008.03.056>
- Naish, T., Powell, R., Levy, R., Wilson, G., Scherer, R., Talarico, F., et al. (2009). Obliquity-paced Pliocene West Antarctic Ice Sheet oscillations. *Nature*, 458(7236), 322–328. <https://doi.org/10.1038/nature07867>
- Nakada, M., Okuno, J., Lambeck, K., & Purcell, A. (2015). Viscosity structure of Earth's mantle inferred from rotational variations due to GIA process and recent melting events. *Geophysical Journal International*, 202(2), 976–992. <https://doi.org/10.1093/gji/ggv198>
- Neron de Surgy, O., & Laskar, J. (1997). On the long term evolution of the spin of the Earth. *Astronomy and Astrophysics*, 318, 975–989.
- O'Neil, J. R., Clayton, R. N., & Mayeda, T. K. (1969). Oxygen isotope fractionation in divalent metal carbonates. *The Journal of Chemical Physics*, 51(12), 5547–5558. <https://doi.org/10.1063/1.1671982>
- Pälike, H., Norris, R. D., Herrle, J. O., Wilson, P. A., Coxall, H. K., Lear, C. H., et al. (2006). The heartbeat of the Oligocene climate system. *Science*, 314(5807), 1894–1898. <https://doi.org/10.1126/science.1133822>
- Pälike, H., & Shackleton, N. J. (2000). Constraints on astronomical parameters from the geological record for the last 25 Myr. *Earth and Planetary Science Letters*, 182(1), 1–14. [https://doi.org/10.1016/S0012-821X\(00\)00229-6](https://doi.org/10.1016/S0012-821X(00)00229-6)
- Pekar, S. F., & DeConto, R. M. (2006). High-resolution ice-volume estimates for the early Miocene: Evidence for a dynamic ice sheet in Antarctica. *Paleogeography, Paleoclimatology, Paleoecology*, 231(1–2), 101–109. <https://doi.org/10.1016/j.palaeo.2005.07.027>
- Peltier, W. R. (1974). The impulse response of a Maxwell Earth. *Reviews of Geophysics*, 12(4), 649–669. <https://doi.org/10.1029/rg012i004p00649>
- Peltier, W. R. (1976). Glacial-isostatic adjustment—II. The inverse problem. *Geophysical Journal International*, 46(3), 669–705. <https://doi.org/10.1111/j.1365-246x.1976.tb01253.x>
- Peltier, W. R. (1983). Constraint on deep mantle viscosity from lagoon acceleration data. *Nature*, 304(5925), 434–436. <https://doi.org/10.1038/304434a0>
- Peltier, W. R. (1985). The LAGEOS constraint on deep mantle viscosity: Results from a new normal mode method for the inversion of viscoelastic relaxation spectra. *Journal of Geophysical Research: Solid Earth*, 90(B11), 9411–9421. <https://doi.org/10.1029/jb090ib11p09411>
- Peltier, W. R. (2004). Global glacial isostasy and the surface of the ice-age Earth: The ICE-5G (VM2) model and grace. *Annual Review of Earth and Planetary Sciences*, 32(1), 111–149. <https://doi.org/10.1146/annurev.earth.32.082503.144359>
- Peltier, W. R. (2015). *The history of the Earth's rotation: Impacts of deep Earth physics and surface climate variability*. Elsevier.
- Peltier, W. R., & Andrews, J. T. (1976). Glacial-isostatic adjustment—I. The forward problem. *Geophysical Journal International*, 46(3), 605–646. <https://doi.org/10.1111/j.1365-246x.1976.tb01251.x>
- Peltier, W. R., Argus, D., & Drummond, R. (2015). Space geodesy constrains ice age terminal deglaciation: The global ICE-6G_C (VM5a) model. *Journal of Geophysical Research: Solid Earth*, 120(1), 450–487. <https://doi.org/10.1002/2014jb011176>
- Peltier, W. R., & Jiang, X. (1994). The precession constant of the Earth: Variations through the ice-age. *Geophysical Research Letters*, 21(21), 2299–2302. <https://doi.org/10.1029/94gl02058>
- Pendea, I. F., Costopoulos, A., Nielsen, C., & Chmura, G. L. (2010). A new shoreline displacement model for the last 7 ka from eastern James Bay, Canada. *Quaternary Research*, 73(3), 474–484. <https://doi.org/10.1016/j.yqres.2010.02.001>
- Pico, T., Creveling, J., & Mitrovica, J. (2017). Sea level records from the U.S. mid-Atlantic constrain Laurentide ice sheet extent during marine isotope stage 3. *Nature Communications*, 8(1), 1–6. <https://doi.org/10.1038/ncomms15612>
- Pollard, D., & DeConto, R. M. (2005). Hysteresis in Cenozoic Antarctic ice-sheet variations. *Global and Planetary Change*, 45(1–3), 9–21. <https://doi.org/10.1016/j.gloplacha.2004.09.011>
- Pollard, D., & DeConto, R. M. (2009). Modeling West Antarctic Ice Sheet growth and collapse through the past 5 Myr. *Nature*, 458(7236), 329–332. <https://doi.org/10.1038/nature07809>
- Pollard, D., DeConto, R. M., & Alley, R. B. (2015). Potential Antarctic ice sheet retreat driven by hydrofracturing and ice cliff failure. *Earth and Planetary Science Letters*, 412, 112–121. <https://doi.org/10.1016/j.epsl.2014.12.035>
- Raymo, M. E., Kozdon, R., Evans, D., Lisiecki, L., & Ford, H. L. (2018). The accuracy of mid-Pliocene $\delta^{18}\text{O}$ -based ice volume and sea level reconstructions. *Earth-Science Reviews*, 177, 291–302.
- Raymo, M. E., Mitrovica, J., O'Leary, M. J., DeConto, R. M., & Hearty, P. J. (2011). Departures from eustasy in Pliocene sea level records. *Nature Geoscience*, 4(5), 328–332. <https://doi.org/10.1038/ngeo1118>
- Rocchi, S., LeMasurier, W. E., & Di Vincenzo, G. (2006). Oligocene to Holocene erosion and glacial history in Marie Byrd Land, West Antarctica, inferred from exhumation of the Dorrel Rock intrusive complex and from volcano morphologies. *Geological Society of America Bulletin*, 118(7–8), 991–1005. <https://doi.org/10.1130/b25675.1>
- Rose, K. C., Ferraccioli, F., Jamieson, S. S., Bell, R. E., Corr, H., Creyts, T. T., et al. (2013). Early East Antarctic Ice Sheet growth recorded in the landscape of the Gamburtsev Subglacial Mountains. *Earth and Planetary Science Letters*, 375, 1–12. <https://doi.org/10.1016/j.epsl.2013.03.053>

- Roy, K., & Peltier, W. (2011). Grace era secular trends in Earth rotation parameters: A global-scale impact of the global warming process? *Geophysical Research Letters*, 38(10). <https://doi.org/10.1029/2011gl047282>
- Roy, K., & Peltier, W. (2015). Glacial isostatic adjustment, relative sea level history, and mantle viscosity: Reconciling relative sea level model predictions for the U.S. East Coast with geological constraints. *Geophysical Journal International*, 201(2), 1156–1181. <https://doi.org/10.1093/gji/ggv066>
- Roy, K., & Peltier, W. (2017). Space-geodetic and water level gauge constraints on continental uplift and tilting over North America: Regional convergence of the ICE-6G_C (VM5a/VM6) models. *Geophysical Journal International*, 210(2), 1115–1142. <https://doi.org/10.1093/gji/ggx156>
- Sabadini, R., Vermeersen, B., & Cambiotti, G. (2016). *Global dynamics of the Earth*. Springer.
- Shackleton, N. J. (1975). Paleotemperature history of the Cenozoic and the initiation of Antarctic glaciation: Oxygen and carbon isotope analyses in DSDP sites 277, 279, and 281. *Initial Reports of Deep Sea Drilling Project*, 29, 743–756.
- Shackleton, N. J., Backman, J., Zimmerman, H., Kent, D. V., Hall, M., Roberts, D. G., et al. (1984). Oxygen isotope calibration of the onset of ice-raftering and history of glaciation in the North Atlantic region. *Nature*, 307(5952), 620–623. <https://doi.org/10.1038/307620a0>
- Shakun, J. D., Corbett, L. B., Bierman, P. R., Underwood, K., Rizzo, D. M., Zimmerman, S. R., et al. (2018). Minimal East Antarctic Ice Sheet retreat onto land during the past 8 Myr. *Nature*, 558(7709), 284–287. <https://doi.org/10.1038/s41586-018-0155-6>
- Sorlien, C. C., Luyendyk, B. P., Wilson, D. S., Decesari, R. C., Bartek, L. R., & Diebold, J. B. (2007). Oligocene development of the West Antarctic Ice Sheet recorded in Eastern Ross Sea Strata. *Geology*, 35(5), 467–470. <https://doi.org/10.1130/g23387a.1>
- Sosdian, S., & Rosenthal, Y. (2009). Deep-sea temperature and ice volume changes across the Pliocene-Pleistocene climate transitions. *Science*, 325(5938), 306–310. <https://doi.org/10.1126/science.1169938>
- Spada, G., Barletta, V. R., Klemann, V., Riva, R., Martinec, Z., Gasperini, P., et al. (2011). A benchmark study for glacial isostatic adjustment codes. *Geophysical Journal International*, 185(1), 106–132. <https://doi.org/10.1111/j.1365-246x.2011.04952.x>
- Spada, G., & Melini, D. (2015). *SELEN: A program for solving the “sea level equation” — Manual version 1.2, December 2015, Computational Infrastructure for Geodynamics (CIG)*.
- Spada, G., & Melini, D. (2019). SELEN⁴ (SELEN version 4.0): A Fortran program for solving the gravitationally and topographically self-consistent sea level equation in glacial isostatic adjustment modeling. *Geoscientific Model Development*, 12(12), 5055–5075. <https://doi.org/10.5194/gmd-12-5055-2019>
- Spada, G., Melini, D., Galassi, G., & Colleoni, F. (2012). *Modeling sea level changes and geodetic variations by glacial isostasy: The improved SELEN code*. arXiv preprint arXiv:1212.5061.
- Spada, G., & Stocchi, P. (2007). SELEN: A Fortran 90 program for solving the “sea level equation”. *Computers & Geosciences*, 33(4), 538–562. <https://doi.org/10.1016/j.cageo.2006.08.006>
- Stacey, F. D., & Davis, P. M. (2008). *Physics of the Earth*. Cambridge University Press.
- Stephenson, F. R. (2008). *Historical eclipses and Earth’s rotation*. Cambridge University Press.
- Stephenson, F. R., Morrison, L. V., & Smith, F. (1995). Long term fluctuations in the Earth’s rotation: 700 BCE to CE 1990. *Philosophical Transactions of the Royal Society of London. Series A: Physical and Engineering Sciences*, 351(1695), 165–202.
- Tegmark, M. (1996). An icosahedron-based method for pixelizing the celestial sphere. *The Astrophysical Journal*, 470(2), L81–L84. <https://doi.org/10.1086/310310>
- Thomson, D. J. (1990). Quadratic-inverse spectrum estimates: Applications to paleoclimatology. *Philosophical Transactions of the Royal Society of London. Series A: Physical and Engineering Sciences*, 332(1627), 539–597.
- Tripathi, A., & Darby, D. (2018). Evidence for ephemeral middle Eocene to early Oligocene Greenland glacial ice and pan-Arctic sea ice. *Nature communications*, 9(1), 1–11. <https://doi.org/10.1038/s41467-018-03180-5>
- Westerhold, T., Marwan, N., Drury, A. J., Liebrand, D., Agnini, C., Anagnostou, E., et al. (2020). An astronomically dated record of Earth’s climate and its predictability over the last 66 Myr. *Science*, 369(6509), 1383–1387. <https://doi.org/10.1126/science.aba6853>
- Whitehouse, P. L., Bentley, M. J., Milne, G. A., King, M. A., & Thomas, I. D. (2012). A new glacial isostatic adjustment model for Antarctica: Calibrated and tested using observations of relative sea level change and present-day uplift rates. *Geophysical Journal International*, 190(3), 1464–1482. <https://doi.org/10.1111/j.1365-246x.2012.05557.x>
- Winnick, M. J., & Caves, J. K. (2015). Oxygen isotope mass-balance constraints on Pliocene sea level and East Antarctic Ice Sheet stability. *Geology*, 43(10), 879–882. <https://doi.org/10.1130/g36999.1>
- Wu, P., & Peltier, W. R. (1982). Viscous gravitational relaxation. *Geophysical Journal International*, 70(2), 435–485. <https://doi.org/10.1111/j.1365-246x.1982.tb04976.x>
- Yoder, C. (1995). Astrometric and geodetic properties of Earth and the solar system. *Wiley Online Library*, 1(No. 88).
- Yoder, C., Williams, J., Dickey, J., Schutz, B., Eanes, R., & Tapley, B. (1983). Secular variation of Earth’s gravitational harmonic J_2 coefficient from lagoon and nontidal acceleration of Earth rotation. *Nature*, 303(5920), 757–762. <https://doi.org/10.1038/303757a0>
- Zachos, J. C., Dickens, G. R., & Zeebe, R. E. (2008). An early Cenozoic perspective on greenhouse warming and carbon-cycle dynamics. *Nature*, 451(7176), 279–283. <https://doi.org/10.1038/nature06588>